International Journal of Earth Sciences
https://doi.org/10.1007/s00531-020-01942-5

ORIGINAL PAPER

Employing geochemistry and geochronology to unravel genesis and tectonic setting of iron oxide-apatite deposits of the Bafq-Saghand metallogenic belt, Central Iran

Seyed Afshin Majidi[1,2] · Jafar Omrani[1] · Valentin R. Troll[3] · Franz A. Weis[3] · Abdolrahim Houshmandzadeh[4] · Ehsan Ashouri[5] · Nima Nezafati[2] · Sun-Lin Chung[6]

Received: 5 January 2020 / Accepted: 29 September 2020

Abstract

The Bafq-Saghand metallogenic belt is located in the central part of the Kerman–Kashmar tectonic zone and contains 39 individual occurrences of iron oxide-apatite ± REE mineralizations. These mineral concentrations, e.g., Chadormalu, Choghart, Sechahun, and Esfordi, comprise a total of ~ 1500 million tons of iron ore with an average grade of ~ 55% Fe. In terms of origin, time, and geodynamic setting, several modes of formation have been suggested for these ore deposits, including magmatic, hydrothermal, and banded iron formation scenarios. In the present study, the tectonic setting and metallogeny of iron oxide-apatites of the Bafq-Saghand belt are investigated utilizing trace element geochemistry, age dating, and oxygen isotope analyses. The geochemical characteristics of apatite and magnetite and the $\delta^{18}O$ values of magnetite (from −0.1 to +2.2 ‰) indicate a dominantly magmatic-hydrothermal ($\delta^{18}O > +0.9$ ‰) formation process, although primary magmatic mineralizations were locally leached and hydrothermally redeposited (e.g., samples with $\delta^{18}O < +0.9$ ‰). The Cambrian volcano-sedimentary host rocks to the mineralization is intruded by calc-alkaline tonalite, trondhjemite, granodioritic, dioritic, and granitic rocks that formed in association with subduction of the Proto-Tethys Ocean under the Gondwana supercontinent in the Neoproterozoic to Early Cambrian (525–547 Ma). Additionally, a later geodynamic episode produced intrusions of alkaline syenite and monzosyenite bodies during a continental rifting event. We provide new geochronological constraints for these younger alkaline igneous rocks that document a temporal range from 421 to 447 Ma for their intrusion. In combination with the previously reported overlapping ages of the older calc-alkaline magma bodies (525–547 Ma) with the volcano-sedimentary host rock (528 Ma) and the iron oxide mineralization (510–539 Ma), we can now exclude continental rifting as a geodynamic processes that is linked to ore formation in the region. Our results corroborate that the Bafq iron ore mineralization formed during subduction of the Proto-Tethys Ocean under the Gondwana supercontinent in a near surface continental margin setting.

Keywords Kiruna-type ore deposits · Bafq-saghand metallogenic belt · Central Iran zone · Calc–alkaline magmatism · Alkaline magmatism · Geochronology · Geochemistry

✉ Seyed Afshin Majidi
afshinmajidi@gmail.com

[1] Geological Survey of Iran, Mehraj Bd, Tehran, Iran

[2] Department of Geology and Geophysics, Islamic Azad University, Science and Research Branch, Tehran, Iran

[3] Department of Earth Science, Section for Natural Resources and Sustainable Development, Uppsala University, Villavägen 16, 752 36 Uppsala, Sweden

[4] Pars Kani Mineral Industries Research and Development, Tehran, Iran

[5] Department of Mining Engineering, Isfahan University of Technology, 84156-83111 Isfahan, Iran

[6] Department of Geosciences, National Taiwan University, Taipei, Taiwan

Published online: 27 October 2020

Introduction

Iron is the most important metal for modern industry and will remain so for many decades to come (e.g., Arndt et al. 1977). Iron is sourced from several types of ore deposit, with Kiruna-type iron ores being one of the important deposit types for iron at present. Kiruna-type iron-apatite deposits are widely classified as part of the IOCG group of ore deposits, a concept that was introduced after the exploration of the Olympic Dam deposit in Australia (Roberts and Hudson 1983; Meyer 1988; Porter 2011; Dmitrijeva et al. 2018; Simon et al. 2018). Later workers gradually departed from this classification and iron-apatite deposits may represent a separate and self-standing deposit type (Hitzman et al. 1992; Williams et al. 2005; Groves et al. 2010; Jonsson et al. 2013; Troll et al. 2019). More specifically, magnetite-apatite deposits come typically in two major categories: (1) magnetite-ilmenite enriched apatites (i.e., nelsonite with almost 30% apatite) often associated with anorthosite or (2) low-Ti iron oxide-apatite deposits with high amounts of phosphate known as Kiruna-type (Williams et al. 2005; Groves et al. 2010). Genesis of the first category may be related to liquid immiscibility between silicate magmas and Fe–Ti–P melts (Philpotts 1967; Zhou et al. 2013); however, partial melting of Fe and P enriched crustal rocks or extreme crystal fractionation were also previously proposed (Kolker 1982; Barton and Johnson 1996; Naslund et al. 2002). Regarding Kiruna-type iron oxide-apatite deposits, their often magmatic textures and the usual association with sub-alkaline igneous rocks led to a range of magmatic fractionation and immiscibility models to explain their origin for this deposits type (e.g., Nyström and Henriquez 1994; Clark and Kontak 2004; Hou et al. 2011; Yu et al. 2011; Tornos et al. 2017; Simon et al. 2018; Sarlus et al. 2020). In addition, on the basis of oxygen isotope and trace element studies, a high-temperature magmatic to magmatic-hydrothermal origin was suggested for Kiruna-type deposits (Nyström et al. 2008; Jonsson et al. 2013; Broughm et al. 2017; Tornos et al. 2017; Troll et al. 2019; Peters et al. 2020) although based on textural and geochemical grounds, hydrothermal processes are also widely recorded in such deposits (e.g., Hitzman et al. 2000; Rojas et al. 2018; Simon et al. 2018; Hu et al. 2020). This aspect is underpinned by fluid inclusion studies that document hydrothermally processes at work (Jami et al. 2007; Vapnik et al. 2007; Heidarian et al. 2017; Nikolenko et al. 2018), leading some workers to put forward a sedimentary exhalative origin for several Kiruna-type deposits (Parák 1975; Aftabi et al. 2009; Mohseni and Aftabi 2015). Most recently, however, the main discussion in respect to Kiruna-type deposits centered around whether a purely ortho-magmatic origin (i.e., magma and magmatic fluids at high temperatures) (e.g., Frietsch 1978; Henríquez and Martin 1978; Nyström and Henríquez 1994; Barton and Johnson 1996; Knipping et al. 2015a, b, Ovalle et al. 2018; Simon et al. 2018; Troll et al. 2019) or a hydrothermal and metasomatic origin at medium to low temperature (Bookstorm et al. 2011; Dare et al. 2014; Westhues et al. 2016; Westhues et al. 2016, 2017a; b; Deymar et al. 2018) applies.

The Bafq-Saghand metallogenic belt within the Kashmar–Kerman Tectonic Zone is located between the Yazd and Tabas structural blocks in Central Iran (Haghipour and Pelissier 1977; Ramezani and Tucker 2003) (Fig. 1) and hosts 39 individual iron mineralizations that contain more than 1500 million tons of iron ore (Fig. 2). The ore content of the individual deposits varies between 10 and 400 million tons at an average grade of ~ 55 wt. % Fe (Förster and Jafarzadeh 1994; Torab 2008) and different models have been put forward to explain the Bafq-Saghand iron ore mineralization. These comprise an association of the ore deposits with carbonatite magmatism (Darvishzadeh 1983; Samani 1988; Förster and Borumandi 1971) or with alkaline magmatism (Mokhtari et al. 2013), with magmatic crystallization and immiscible magmatic processes in connection with calc-alkaline magmatism (Förster and Jafarzadeh 1994; Williams and Houshmandzadeh 1966; Mücke and Younessi 1994; Moore and Modabberi 2003), hydrothermal fluid processes and hydrothermal overprint associated with calc-alkaline magmatic activity (Daliran 2002; Jami et al. 2007; Torab and Lehman 2007; Bonyadi et al. 2011; Heidarian et al. 2017; Ghazi et al. 2019), or banded iron formation style sedimentary processes (Aftabi et al. 2009. Mohseni and Aftabi 2012, 2015). In addition to the metallogenic discussion, two rival possibilities for the tectonic setting of ore forming events are also widely discussed: (1) a within plate rifting event (Berberian and King 1981) and (2) a subduction related arc setting (Ramezani and Tucker 2003).

In this study we aim to resolve (a) the petrogenetic association of the iron oxide-apatite deposits in the Bafq-Saghand metalogenic belt using trace elements of apatite and magnetite and oxygen isotopes in magnetite from four individual iron deposits in the region (Chadormalu, Choghart, Se-Chahun and Esfordi) and (b) resolve the timing and tectonic setting of ore formation, through geochemical whole rock analysis and U–Pb zircon dating of so far undated alkaline intrusive rocks in the region.

Geological background

The microcontinents of the western parts of Central Iran were described individually by Takin (1972) and comprise three separate fault-bound blocks of N–S orientation (the Lut, Tabas and Yazd Blocks) (Fig. 1b). The Tabas and

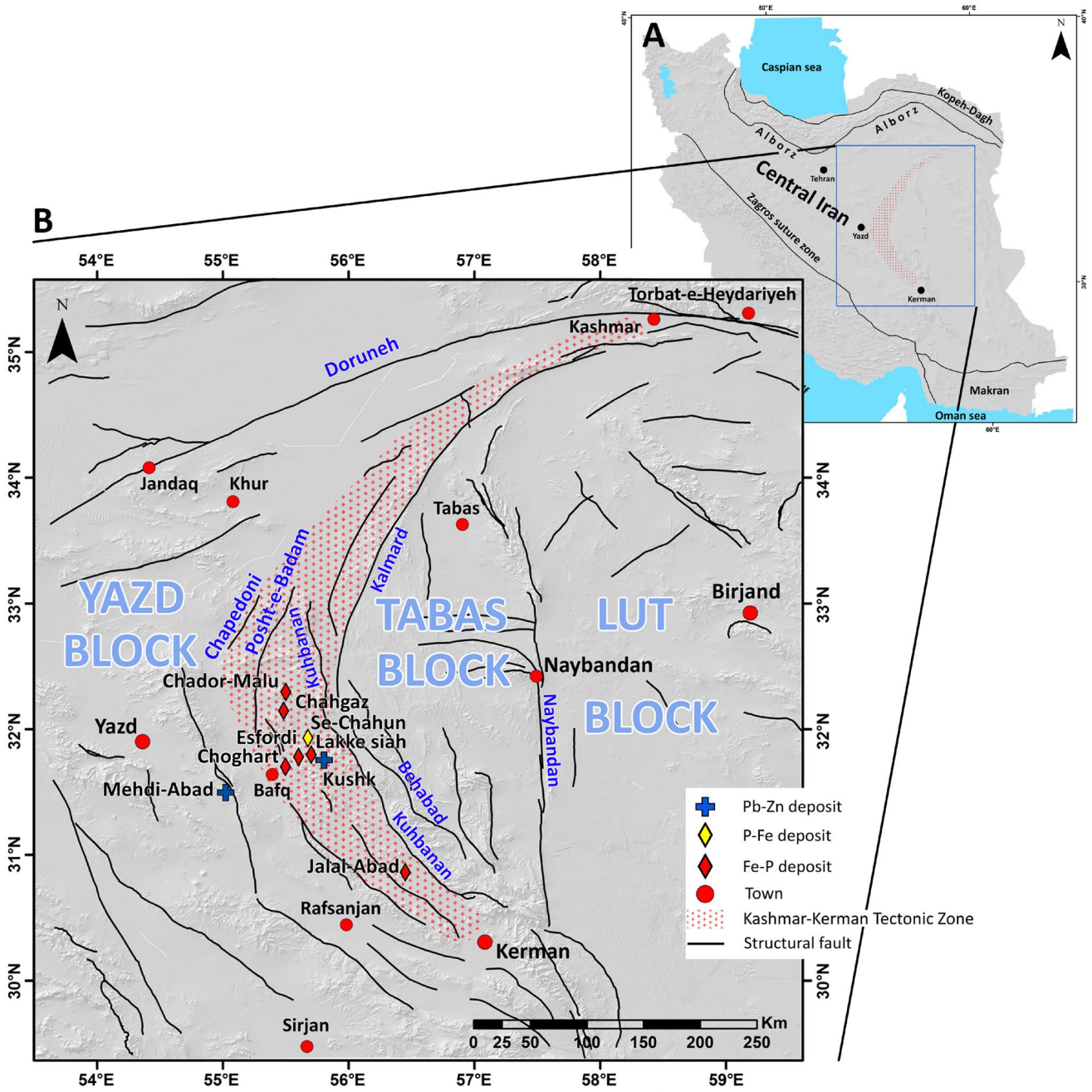

Fig. 1 The Bafq-Saghand metallogenic belt lies within the Kashmar–Kerman Tectonic Zone (red stippled area), which is located between the Yazd and Tabas structural blocks in central Iran (modified after, Haghipour and Pelissier 1977; Ramezani and Tucker 2003)

Yazd blocks are separated by a structural belt defined as the Kashmar–Kerman tectonic zone. The Kashmar–Kerman tectonic zone includes metamorphic basement units covered by Mesozoic-Cenozoic units. The Bafq-Saghand belt is located in central part of the Kashmar–Kerman tectonic zone, which provides remarkable exposures of the deeper crustal levels of Upper Neoproterozoic and Lower Paleozoic rocks (Fig. 2) (Haghipour et al. 1977; Soheili and Mahdavi 1991; Ramezani and Tucker 2003). The Bafq-Saghand belt contains sedimentary, metamorphic, and volcanoclastic units of the Late Neoproterozoic to Early Cambrian Tashk complex (627–533 Ma), which represent the oldest rock series of the Bafq-Saghand belt (Figs. 2, 3) (Ramezani and Tucker 2003).In detail,, the metamorphic units of the Tashk Complex comprise migmatites, amphibolites, gneiss, schists, marble, and quartzites along with carbonate and volcano-sedimentary sub-units that belong to the Boneh-Shurow (617–544 ± 7 Ma). Poshteh-Badam (likely Neoproterozoic),

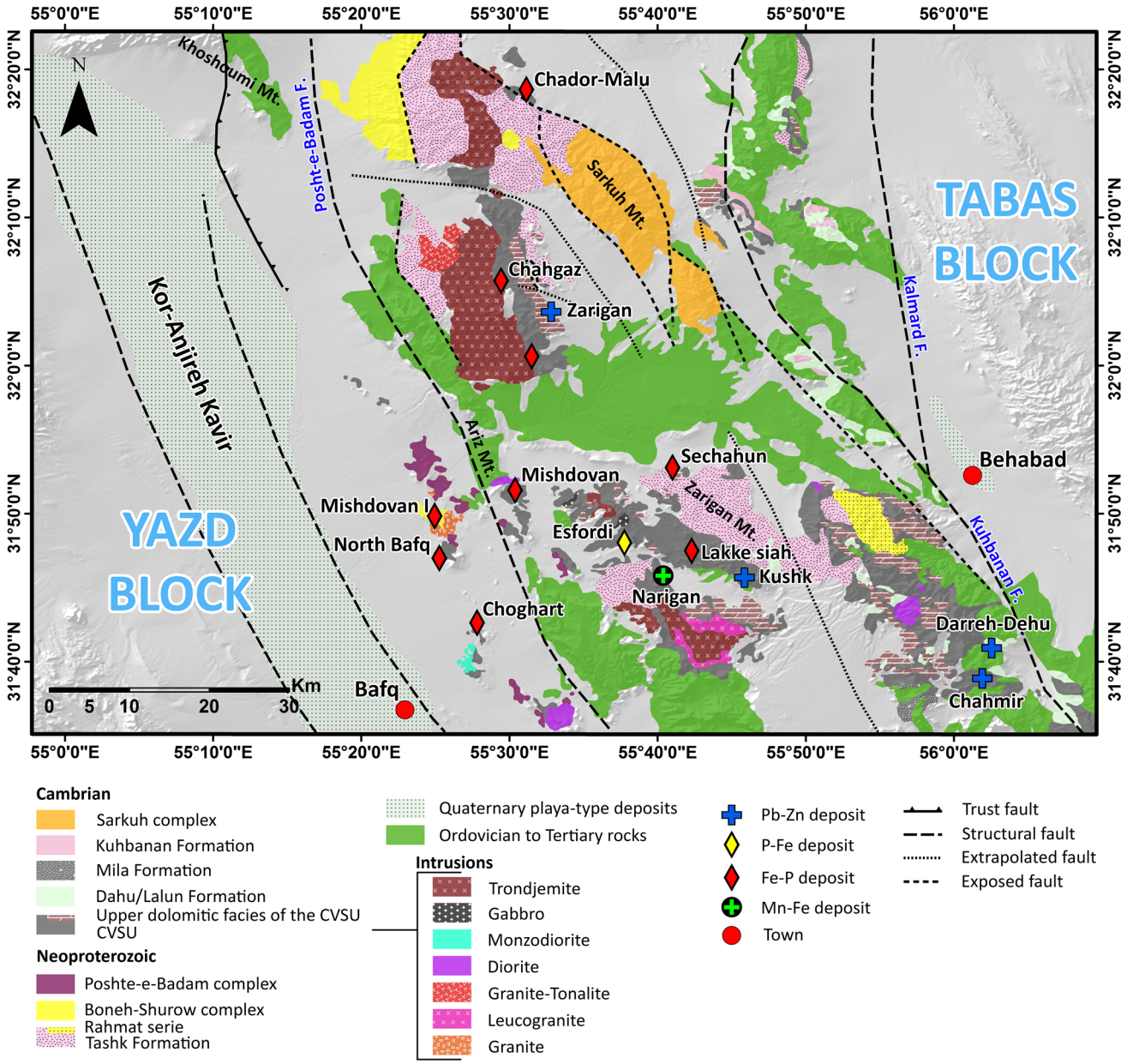

Fig. 2 Simplified geological map of the Bafq-Saghand zone with location of the main ore deposits. Iron ore deposits are marked with diamond symbols. The estimated iron ore tonnage is over 1500 million tons

and Sarkuh (likely Neoproterozoic—Early Cambrian) metamorphic complexes (Haghipour et al. 1977; Ramezani and Tucker 2003) (Figs. 2, 3).

The overlaying Cambrian Volcano-Sedimentary Unit hosts the iron oxide-apatite ores of the Bafq-Saghand belt (Figs. 2, 3) (Huckriede et al. 1962; Stöcklin 1968; Haghipour and Pelissier 1977). This unit comprises felsic to intermediate volcanic rocks, dolomitic limestones with occasional gypsum interlayers (Ramezani and Tucker 2003), and some shale-sandstone sub-units (Haghipour and Pelissier 1977) that are widely exposed throughout the Bafq-Saghand zone (Fig. 2). The Cambrian Volcano-Sedimentary Unit displays a thickness of ~ 1500 m. although deformation processes and hydrothermal activities occurred along the boundary of the Cambrian Volcano-Sedimentary Unit (Fig. 2) (Ramezani and Tucker 2003).

The Cambrian Volcano-Sedimentary Unit that hosts the iron oxide-apatite ore deposits is also known as the Saghand formation (Samani 1993), the Rizu-Dezu series (Berberian and King 1981) or the Esfordi formation (Förster and Borumandi 1971). The Cambrian Volcano-Sedimentary Unit is intruded by a series of calc-alkaline intrusions and most of the

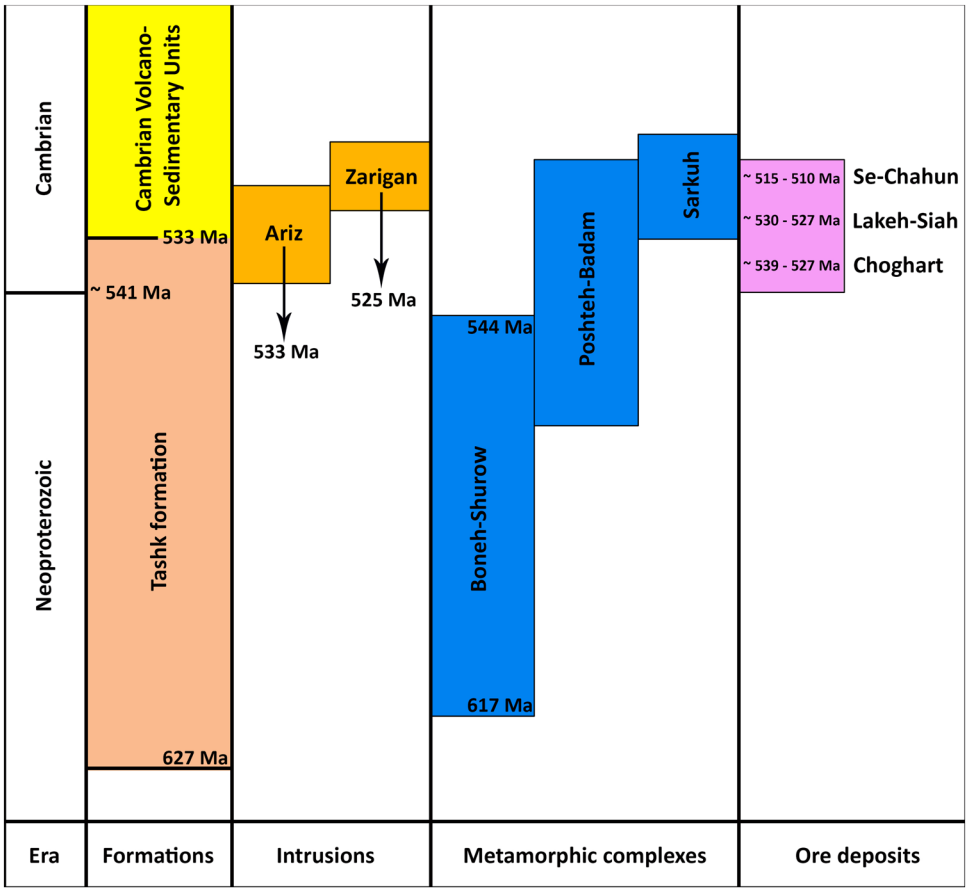

Fig. 3 Schematic stratigraphical chart of the Neoproterozoic-Cambrian Bafq-Saghand iron belt

volcanic rocks of the Cambrian Volcano-Sedimentary Unit are derived from the three calc-alkaline igneous complexes that are, based on geochemical characteristics, felsic volcanic and magmatic rocks of an arc type magmatic setting (Ramezani and Tucker 2003; Jami 2005). The three calc-alkaline magmatic complexes that intruded the Bafq-Saghand belt comprise (1) the Cambrian Ariz granitoids (533 ± 1 Ma), (2) the Cambrian Zarigan leucogranites (525–526 ± 1 Ma), and (3) the post-metamorphic Eocene Khoshumi granitoids (44.3 ± 1 to 43.4 ± 0.2 Ma) (Ramezani and Tucker 2003) (Figs. 2, 3). The Cambrian Ariz complex is intruded by the Zarigan leucogranite complex, which comprises the Zarigan and the Narigan intrusive granitic massive rocks (525 ± 7 Ma), diabase dykes, the Douzakh–Darreh leucogranites (526 ± 1 Ma), and the Sefid granite (525 Ma) (Ramezani and Tucker 2003). The Narigan granite sub-complex, part of the Cambrian Zarigan leucogranite complex, is located 6 km from the Esfordi deposit (Ramezani and Tucker 2003) and covers 50 km^2 square kilometers of surface area (Jami 2005). Boomery (2012) described the Narigan intrusive body in the Northern part of the Esfordi deposit as an alkaline syenite body. According to field observations, this syenite body is also exposed in the Southern part of Lake-Siah deposit (Valizade and Sharifi 2004; Mokhtari et al. 2013) as well as in the Eastern part of Narigan village (Majidi 2015). The Zarigan intrusive body, locally also known as Chadormalu and Mishdowan granite (Daliran 1990; Torab and Lehman 2007), is a shallow (Ramezani and Tucker 2003) to semi-deep (Daliran 1990) white-colored body of aphanitic tonalite-trondhjemite character (Ramezani and Tucker 2003). The body was injected into the Tashk formation and the Cambrian Volcano-Sedimentary Unit and is mostly of granitic to granodioritic composition. In the South-South Eastern parts of the Bafq-Saghand belt, local diorites, as part of the Cambrian granitoids complex, are stratigraphically followed by rhyolite and rhyolitic tuffs (Early Cambrian) (Soheili and Mahdavi 1991; Niktabar and Rashidnejad Omran 2018). The Eocene post-metamorphism activity comprises the Khoshumi granite (44.3 ± 1 Ma) and the Daranjir diorite (43.4 ± 0.2), the former of which intruded into the Chapedony core complex (Ramezani and Tucker 2003) (see Fig. 2).

Ore deposit geology

The Bafq-Saghand metallogenic belt contains, amongst several others, the Choghart, Chadormalu, Se-Chahun and Esfordi iron-apatite deposits (Fig. 2) that are hosted within the Cambrian Volcano-Sedimentary Unit. These

iron oxide-apatite deposits are present as massive, and as vein and stockwork type associations. Specifically, the iron ores occur as regular shaped domes of mostly massive and lenticular-shaped magnetite concentrations surrounded by veined magnetite-bearing host rocks. Magnetite is the most common ore mineral; however, it is often martitised. In addition, actinolite and apatite minerals are widespread within the Bafq-Saghand ores (Fig. 4). The massive magnetite bodies surrounded by magnetite-actinolite-apatite stockworks often show gradual boundaries with the surrounding host rock, and where sharp boundaries are present, they usually have structural (faulted) controls. Textural/mineralogical zoning is usually visible from the central part of the massive ore deposits towards the rims and apatite intergrowths is common within the magnetite bodies. Brecciated rims, large crystals of apatite* and widespread martitisation is ubiquitous (Torab and Lehman 2007). Microscopic studies indicate that granular brecciated textures contain subhedral to euhedral magnetite grains of different sizes with martitisation visible along fractures and grain boundaries due to subsequent hydrothermal fluid overprint (Torab and Lehman 2007). In addition to martitisation, individual crystals and bladed aggregates of presumably primary hematite are also visible within some of the studied deposits (Torab and Lehman 2007). The brecciated ore is usually of low grade and is composed of magnetite ± hematite + apatite + actinolite + quartz and calcite. Phenocrysts of quartz and feldspar become increasingly less abundant from the brecciated zone toward the central part of the ore bodies. Dolomitic parts of the country rocks that are occasionally affected by ore deposition can show alkaline metasomatism (Fig. 4). The carbonated matrix is then converted into actinolite and portions of the associated volcanic host rocks can be pinkish as a result of sodic, potassic and possibly calcic hydrothermal overprint (Fig. 4). In some of the iron-apatite deposits (e.g., Esfordi, Gazestan and Zarigan), apatite veins occur along with actinolites and hematites. The P_2O_5 grade of these apatite veins ranges between 15 and 35 wt. % P_2O_5.

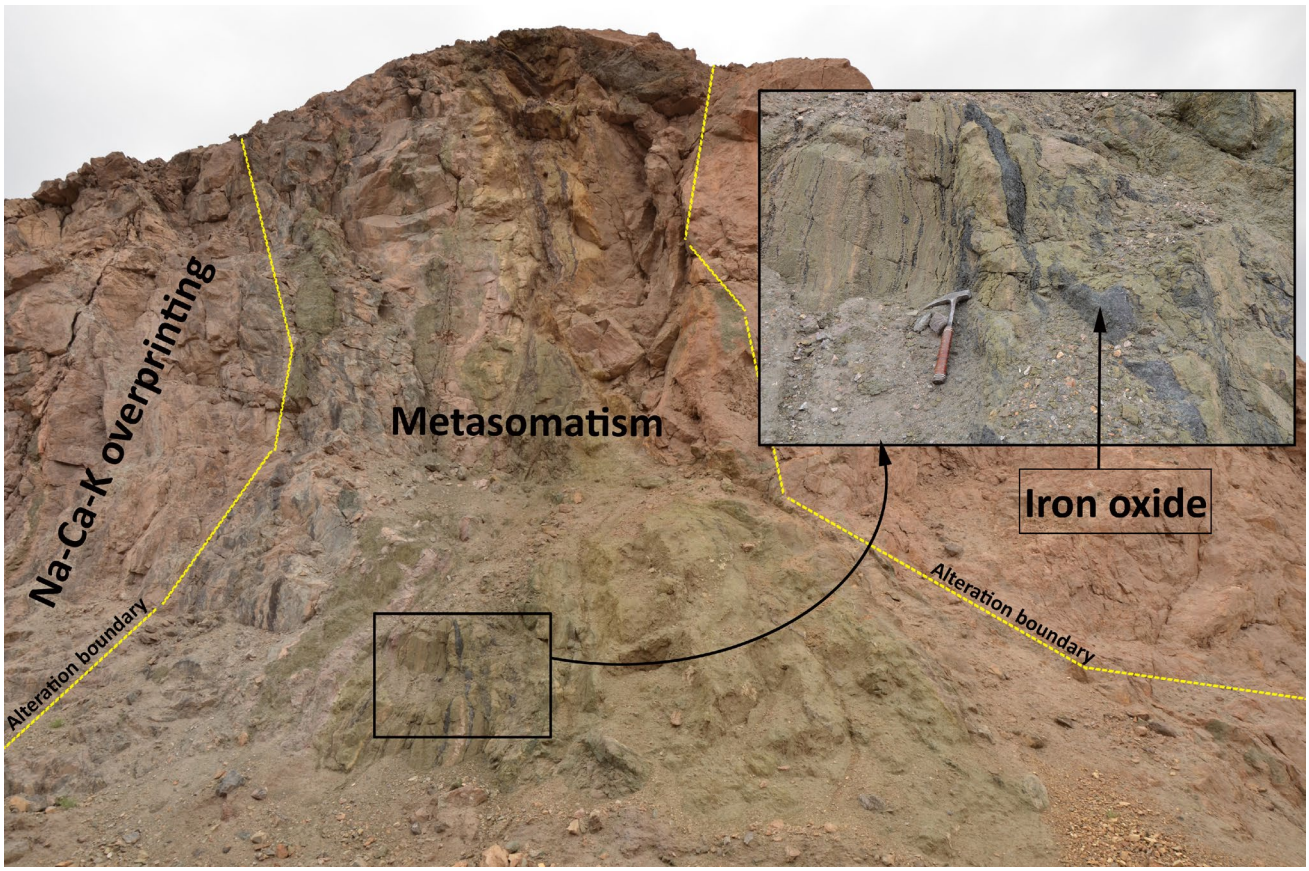

Fig. 4 Field image of metasomatised host rock to the iron oxide-apatite ores in the Bafq-Saghand metallogenic belt. Iron ore veins are visible in lower center of the image and are enlarged in the inset. Dolomitic parts of the Cambrian Volcano-Sedimentary Unit are occasionally alkaline metasomatised. In some cases, volcanic rocks are pinkish as a result of sodic, potassic and possibly calcic hydrothermal activities (See text for details)

Sampling and analytical methods

All collected samples were immediately labeled in the field, stored in plastic bags, and transported to the laboratory at Geological Survey of Iran (GSI) for geochemical analysis. Major oxide elements of igneous rocks, magnetite and apatite samples were analyzed on a MagiX PRO X-ray fluorescence spectrometry (XRF) on fused glass beads at the GSI. Specifically, after crushing, 10 g of each sample was dried for 24 h at 110 °C before conventional gravimetric determination of loss on ignition (LOI) by firing at 1000 °C for at least 2 h. Fusion beads for XRF were prepared using an alkali flux agent comprising 80% lithium tetraborate and 20% lithium metaborate with a sample to flux ratio of 1:2, following the method of Kimura and Yamada (1996). Trace element and REE concentrations were determined with Inductively Coupled Plasma-Mass Spectrometry (ICP-MS) on a Varian 810/820-MS instrument, using the protocol of Jenner et al. (1990) at the applied research center of GSI. Sample powders (0.5 g) were digested using $HF + HNO_3$ mixture (multi acid solution) in high-pressure Teflon beakers for 48 h at ca. 190 °C prior to analysis in the ICP instrument for the quantification of the elements. Rh was used as an internal standard to monitor signal drift during counting. Pure element standards were used for external calibration (Tables 1, 2, 3).

To conduct oxygen isotope analyses, the collected samples were crushed using a jaw crusher and placed in an ultrasonic bath to remove fine dust. After drying, magnetite grains were separated using magnetic separation. The separated magnetite grains were then hand-picked to avoid impurities. Finally, approximately 20 mg of pure magnetite mineral grains was separated per sample for analysis. For oxygen isotopes, both conventional and laser fluorination methods were used. The magnetite separates were analyzed using a conventional silicate line at Cape Town University, South Africa (Harris and Ashwal 2002). Approximately 20 mg (magnetite) sample was reacted with ClF_3, and the liberated O_2 converted to CO_2 using a hot platinized carbon rod. Magnetite was reacted overnight at 600 °C. A sub-set of magnetite separates were analyzed using the laser fluorination analytical process described in Harris and Vogeli (2010). Approximately 5 mg of sample was reacted in the presence of approximately 10 kPa BrF_5 and the purified O_2 was collected onto a 5 A˚ molecular sieve contained in a glass storage bottle. Samples prepared by conventional and by laser fluorination were both analyzed at Cape Town University with a Finnigan DeltaXP mass spectrometer in dual-inlet mode. All data are reported in $\delta^{18}O‰$ are $(R_{sample}/R_{standard} - 1) \times 1000$, and R is the measured ratio (i.e., $^{18}O/^{16}O$) (Table 5). Analysis of standard materials yielded uncertainties of ± 0.15‰.

Samples from alkaline intrusions were subjected to in situ zircon dating. Prior to analysis by LA-ICP MS, euhedral to subhedral zircons with few cracks and inclusions were picked out manually under a binocular microscope and then mounted on epoxy resin and polished for cathodoluminescence (CL) imaging. CL images were used to observing the internal structure of each zircon grain and for selecting suitable positions for laser ablation isotope analysis. U–Pb isotope dating (Table 6) was carried out at the geoscience laboratory of the National University of Taiwan, using a LA ICP-MS. Isotopic ratio of U-Th-Pb was calculated using the (GEMOC) GLITTER 4.0 software. The Pb content was calculated using the Anderson function (Anderson 2002). Additionally, weighted mean was calculated and Concordia dating plots were plotted using Isoplot v.3.0 (Ludwig 2003). A detailed description of the analytical methods applied in this study together with analytical precision can be found in Chiu et al. (2009) and Shao et al. (2015). Standard zircons GJ-1, 91,500 and Plešovice were periodically analyzed to monitor instrumental and analytical conditions and yielded weighted mean $^{206}Pb/^{238}U$ ages of 600.4 ± 0.8 Ma (2σ, $N = 329$), 1065.1 ± 2.7 Ma (2σ, $N = 82$), and 337.2 ± 0.9 Ma (2σ, $N = 81$), respectively, in excellent agreement with the suggested values (Jackson et al. 2004; Sláma et al. 2008; Yuan et al. 2004).

Results

Whole-rock geochemistry of igneous rocks

To better define the geodynamic evolution of the Bafq-Saghand belt, samples from a variety of igneous rocks in the region were collected and analyzed. This included intrusive bodies of the Zarigan, Narigan and Chadormalu granites and the Narigan and Esfordi alkaline syenitic rocks, Cambrian intrusions (e.g., the Ariz Granodiorites), the rhyolitic volcanics (especially the Esfordi and Choghart rhyolites), and various rhyolitic tuffs that crop out over the area. Geochemical data for the calc-alkaline and alkaline rocks of the Bafq-Saghand iron belt are shown in Table 1 and several photographs of samples are presented in Fig. 5. Alkaline samples show a minor range in silica from 54 to 60 wt. % SiO_2. Both Calk-alkaline intrusion and volcanic samples show wider range and roughly the same of silica from 66 to 73.5 wt. %. and 69 to 75 wt. %, respectively. The alkaline samples have relatively high contents of Na_2O (1.5–7.5 wt. %) and K_2O (5.2–9.7 wt. %), as well as Nb (3.75–217 ppm), Ta (0.9–11.5 ppm), Ti (360–6663 ppm), Sr (83–942 ppm), and TREE (208–715 ppm) compared with the calc-alkaline samples that have low K_2O (0.2–5.5 wt.%) and TREE (17–196 ppm), moderate CaO (0.11–3.6 wt.%), but high

Table 1 Main oxide, trace elements and REE analysis result of the Bafq-Saghand igneous rocks

Sample ID	Calc-alkaline rocks										
	Zarigan intrusion										Chador.*
	G.13	G.15	G.19	G.21	G.33	G.38	G38	15Zar-01	15Zar-02	15Zar-03	13.C.23
SiO_2 (wt.%)	68.81	76.26	65.91	76.15	74.67	74.58	77.68	74.96	75.31	74.66	77.06
TiO_2	0.52	0.16	0.69	0.18	0.39	0.31	0.17	0.30	0.20	0.19	0.13
Al_2O_3	14.56	12.57	14.57	12.68	14.99	14.77	12.17	14.65	14.33	14.02	12.55
Fe_2O_3	4.19	1.54	4.54	1.47	0.72	0.78	0.70	0.70	0.70	0.88	1.18
MnO	0.06	0.01	0.06	0.02	0.01	0.01	0.03	0.01	0.03	0.03	0.01
MgO	1.40	0.25	2.10	0.17	0.10	0.12	0.27	0.18	0.10	0.23	0.29
CaO	3.57	1.06	3.43	0.48	0.37	0.84	1.02	0.89	0.90	0.93	0.34
Na_2O	3.58	3.47	3.03	4.22	8.47	7.16	5.26	6.93	6.88	7.14	2.19
K2O	2.86	4.51	4.21	4.92	0.23	1.09	1.30	1.11	1.10	1.50	5.15
P2O5	0.08	0.01	0.16	0.01	0.03	0.04	0.02	0.03	0.04	0.03	0.13
LOI	0.62	0.41	1.41	0.39	0.41	0.57	1.52	0.60	0.53	0.55	1.01
Total	100.24	100.24	100.11	100.71	100.40	100.26	100.13	100.36	100.12	100.16	100.04
FeO[a]	3.77	1.39	4.09	1.32	0.65	0.70	0.63	0.63	0.63	0.63	1.07
Rb (ppm)	83.00	114.00	51.00	4.00	20.00	35.00					86.21
Ba	868.00	648.00	659.00	78.00	341.00	61.00					546.09
Th	8.61	18.36	13.32	1.92	1.44	26.90					15.82
U	0.97	3.64	1.93	0.86	0.89	4.58					2.50
Nb	7.40	7.60	2.90	6.20	5.10	7.20					3.75
Ta	0.49	0.93	0.30	0.63	0.59	0.93					1.82
La	34.40	34.00	44.80	2.72	5.55	1.96					11.55
Ce	67.20	62.50	88.40	3.62	6.83	2.96					24.39
Pr	7.51	6.28	9.44	0.30	0.60	0.32					2.71
Sr	171.00	77.00	38.00	74.00	172.00	25.00					23.24
Nd	27.30	20.50	32.80	0.80	1.70	1.15					10.79
Zr	200.00	118.00	191.00	252.00	224.00	172.00					137.65
Hf	5.89	4.75	7.15	8.74	7.65	7.91					4.62
Sm	5.59	3.92	4.97	0.14	0.23	0.48					3.75
Eu	1.06	0.55	0.70	0.20	0.53	0.11					0.66
Ti	3141	947	1097	2314	1888	992					399
Gd	5.37	3.88	3.65	0.15	0.24	1.38					2.47
Tb	0.82	0.60	0.49	0.02	0.04	0.37					0.49
Ho	nd	nd	nd	nd	nd	nd					1.10
Er	nd	nd	nd	nd	nd	nd					3.27

Table 1 (continued)

Sample ID	Calc-alkaline rocks										
	Zarigan intrusion										Chador.*
	G.13	G.15	G.19	G.21	G.33	G.38	G38	15Zar-01	15Zar-02	15Zar-03	13.C.23
Yb	2.80	3.12	1.65	0.44	0.47	5.56					3.75
Lu	0.40	0.47	0.25	0.08	0.09	0.87					0.95

Sample ID	Calc-alkaline rocks												
	Ariz intrusion						Narigan intrusion						
	Gd.B.01	Gd.B.02	G.B.01	G.B.02	G.B.03	G.B.04	13-C-32	15 N-01	15 N-02	15 N-03	15 N-04	15 N-05	15 N-06
SiO_2 (wt.%)	67.70	69.35	70.65	69.98	69.72	69.24	73.10	74.06	79.39	72.43	76.80	75.40	76.25
TiO_2	0.26	0.35	0.32	0.29	0.33	0.41	0.25	0.25	0.32	0.34	0.22	0.13	0.02
Al_2O_3	20.62	18.40	17.38	17.27	16.96	19.79	13.94	13.71	11.05	14.26	14.52	12.71	13.26
Fe_2O_3	0.93	1.26	0.92	0.95	1.04	0.22	1.46	1.07	0.94	1.72	0.71	1.02	0.29
MnO	0.02	0.01	0.01	0.02	0.03	0.01	0.13	0.02	0.02	0.02	0.04	0.02	0.03
MgO	1.15	0.75	1.85	0.22	0.34	0.32	0.50	0.55	0.36	0.79	0.35	0.14	0.05
CaO	0.11	0.47	0.27	0.43	1.54	0.22	1.31	1.15	0.68	0.90	1.27	0.73	0.92
Na_2O	2.77	4.61	2.06	3.95	3.53	4.45	2.73	4.02	5.77	7.02	4.76	5.31	4.95
K2O	4.12	2.17	4.66	4.71	4.19	4.76	4.28	4.28	0.33	0.46	0.42	3.43	3.28
P2O5	0.04	0.05	0.06	0.04	0.05	0.06	0.08	0.06	0.04	0.07	0.01	0.03	0.02
LOI	1.50	1.50	2.00	1.30	2.50	1.00	1.76	1.15	0.96	1.68	1.21	0.86	0.91
Total	100.03	99.99	100.05	100.03	99.98	100.00	99.54	100.34	99.89	99.69	100.31	99.78	99.98
FeO[a]	0.84	1.13	0.83	0.85	0.94	0.20	1.31	0.96	0.85	1.55	0.64	0.92	0.26
Rb (ppm)							147.76						
Ba							387.63						
Th							13.43						
U							3.39						
Nb							3.75						
Ta							1.17						
La							45.05						
Ce							84.59						
Pr							9.60						
Sr							37.62						
Nd							34.92						
Zr							85.80						
Hf							3.13						
Sm							5.58						

Table 1 (continued)

Sample ID	Calc-alkaline rocks																			
	Ariz intrusion						Narigan intrusion													
	Gd.B.01	Gd.B.02	G.B.01	G.B.02	G.B.03	G.B.04	13-C-32	15 N-01	15 N-02	15 N-03	15 N-04	15 N-05	15 N-06							
Eu							0.96													
Ti							1215													
Gd							5.44													
Tb							0.77													
Ho							0.76													
Er							1.93													
Yb							3.75													
Lu							0.48													
Sample ID	Alkaline rocks																			
	Esfordi syenite					Narigan syenite				Arash syenite										
	Syen.11	13-C-01	13-C-02	13-C-35	13-C-47	13-C-55	Syen.01	Syen.02	Syen.03	ArS-1	ArS-2	ArS-3	ArS-4	ArS-5	ArS-6	ArS-7	ArS-8	ArS-9	ArS-10	ArS-11	ArS-12
SiO_2 (wt.%)	56.89	55.84	59.82	55.82	57.71	59.84	56.55	59.11	54.25	56.16	56.64	56.82	56.89	57.52	57.90	57.99	58.76	56.20	57.90	57.65	59.99
TiO_2	0.19	0.44	0.29	1.38	0.14	0.36	0.06	0.07	0.07	0.06	0.21	0.07	0.23	0.06	0.08	0.23	0.06	0.36	0.30	0.30	0.21
Al_2O_3	19.33	18.32	17.33	16.33	10.06	17.68	25.54	21.27	28.80	19.08	18.83	19.25	19.17	19.74	19.63	20.19	23.67	20.50	18.67	20.73	20.25
Fe_2O_3	4.77	4.04	4.04	7.82	6.30	6.44	0.44	0.40	0.81	4.85	5.30	4.33	5.23	4.67	4.49	5.35	5.35	6.14	5.35	5.85	4.98
MnO	0.13	0.23	0.16	0.14	0.12	0.16	0.05	0.11	0.10	0.30	0.18	0.15	0.15	0.18	0.06	0.15	0.05	0.16	0.14	0.18	0.14
MgO	1.01	0.99	0.48	1.92	8.10	1.02	0.09	0.09	0.18	0.87	1.24	0.09	0.53	0.38	1.08	0.28	0.08	1.62	0.40	3.30	0.36
CaO	1.11	4.45	5.22	3.22	7.85	1.70	4.75	5.59	1.35	2.54	1.91	4.66	2.02	3.53	1.98	1.59	1.05	1.48	2.88	1.59	2.03
Na2O	6.05	3.67	2.34	3.50	3.10	4.33	5.60	6.02	5.90	4.16	6.28	1.46	6.08	1.60	5.76	3.62	3.62	6.47	6.40	2.39	7.49
K2O	7.05	6.85	6.35	5.42	6.28	5.12	5.73	6.10	6.28	6.89	6.81	9.48	7.13	9.34	6.28	8.01	8.27	6.86	6.83	7.68	6.10
P2O5	0.11	0.31	0.36	0.92	0.30	0.33	0.07	0.12	0.05	0.06	0.12	0.05	0.14	0.06	0.06	0.15	0.05	0.15	0.14	0.11	0.13
LOI	3.04	4.28	4.21	2.87	3.49	2.06	4.40	4.90	2.90	1.65	0.85	2.85	0.35	2.32	1.47	nd	nd	nd	nd	nd	0.13
Total	99.68	99.42	99.61	99.35	99.44	99.04	100.04	100.01	99.98	98.42	98.37	99.21	97.92	99.40	98.79	97.56	99.14	99.94	99.01	99.78	101.81
FeO[a]	4.29	3.64	3.63	7.04	5.67	5.80	0.40	0.36	0.73	4.36	4.77	3.90	4.71	4.20	4.04	4.81	4.81	5.52	4.81	5.26	4.48
Rb (ppm)	205.70	153.32	36.85	109.25	26.61	98.90	179.80	154.10	190.10												
Ba	259.20	890.22	117.89	995.90	304.52	1653.36	136.17	155.48	239.01												
Th	32.50	20.75	17.35	10.28	14.21	11.68	29.80	29.20	14.30												
U	7.80	3.04	3.75	1.77	1.27	2.55	5.60	5.70	4.30												
Nb	117.70	5.90	3.75	25.75	3.75	12.19	188.20	217.20	75.50												
Ta	nd	6.51	5.68	5.58	0.89	5.92	11.50	11.50	5.60												

Table 1 (continued)

Sample ID	Alkaline rocks																			
	Esfordi syenite					Narigan syenite				Arash syenite										
	Syen.11	13-C-01	13-C-02	13-C-35	13-C-47	13-C-55	Syen.01	Syen.02	Syen.03	ArS-1	ArS-2	ArS-3	ArS-4	ArS-5	ArS-6	ArS-7	ArS-8	ArS-9	ArS-10	ArS-11	ArS-12
La	71.80	148.79	158.43	115.83	21.41	68.53	189.60	180.40	75.40											
Ce	224.70	255.98	265.40	276.98	63.61	121.83	330.30	318.40	131.70											
Pr	20.40	19.91	19.75	24.46	10.51	10.83	33.79	34.36	12.78											
Sr	243.90	170.60	113.97	243.29	193.32	942.37	85.90	83.60	336.00											
Nd	57.00	61.27	58.71	80.04	54.10	37.75	98.70	105.70	38.80											
Zr	1014.30	435.76	549.46	205.21	53.49	246.25	1035.40	991.90	596.70											
Hf	nd	8.46	8.45	7.39	3.01	4.66	26.10	25.60	15.30											
Sm	7.60	7.53	6.38	10.43	16.43	5.00	12.99	12.93	4.89											
Eu	1.40	2.17	1.74	4.18	1.71	3.21	2.01	1.93	0.80											
Ti	1139	1202	990	6663	870	2480	360	420	420											
Gd	6.50	7.53	7.71	12.88	8.39	5.26	9.28	9.33	3.35											
Tb	1.10	0.98	1.04	1.71	1.77	0.64	1.45	1.37	0.54											
Ho	1.10	0.72	0.83	1.25	2.92	0.52	1.55	1.44	0.47											
Er	2.80	1.57	1.83	3.12	8.19	1.58	4.41	3.95	1.15											
Yb	2.10	3.75	3.75	3.75	14.79	3.75	4.51	4.19	1.31											
Lu	0.30	0.17	0.20	0.40	1.28	0.20	0.70	0.64	0.20											

Sample IDVolcanic rocks																	
	Rhyolite									Rhyolitic tuff							
	Rhy01	Rhy02	13-C-17	13-C-44	Rhy03	Rhy04	Rhy05	Chog Rhy	Esf Rhy	Tuff-01	Tuff-02	Tuff-03	Tuff-04	Tuff-05	Tuff-06	Tuff-07	Tuff-08
SiO_2 (wt.%)	70.14	70.69	72.11	69.28	72.06	74.85	74.21	70.81	72.22	73.30	72.35	74.17	70.76	70.19	73.16	71.62	72.21
TiO_2	0.19	0.19	0.30	0.26	0.25	0.15	0.16	0.20	0.35	0.09	0.20	0.23	0.14	0.18	0.18	0.15	0.14
Al_2O_3	12.14	11.98	12.22	13.03	12.36	9.72	11.57	11.91	15.02	10.37	11.58	12.62	10.48	11.18	12.28	11.84	11.02
Fe_2O_3	1.72	2.05	2.63	2.56	3.14	2.88	2.16	1.74	1.08	0.53	0.82	2.56	1.00	1.50	2.71	2.84	3.12
MnO	0.01	0.03	0.13	0.02	0.04	0.02	0.02	0.03	0.01	0.09	0.04	0.01	0.04	0.05	0.02	0.04	0.06
MgO	0.21	0.63	0.75	0.92	0.59	0.41	0.61	1.10	1.31	0.44	1.43	0.68	2.35	0.87	1.24	0.92	0.94
CaO	1.70	1.83	1.70	1.02	0.86	0.92	1.29	1.92	0.23	2.21	3.15	0.79	2.41	2.78	2.29	3.26	2.61
Na_2O	0.31	0.45	0.39	0.13	6.03	2.82	1.23	5.75	0.22	0.15	0.14	5.27	0.36	0.34	0.51	0.69	0.21
K2O	10.37	9.54	6.69	10.10	2.02	3.64	6.46	1.04	4.91	8.40	5.59	2.64	7.45	8.53	5.18	5.27	7.02
P2O5	0.03	0.04	0.09	0.08	0.08	0.09	0.06	0.16	0.07	0.12	0.06	0.06	0.03	0.05	0.18	0.05	0.04
LOI	2.17	2.07	2.65	1.37	3.11	3.83	2.47	4.95	4.21	3.69	4.81	1.81	4.57	3.32	2.13	3.61	3.25
Total	98.98	99.50	99.65	98.75	100.54	99.33	100.24	99.62	99.62	99.39	100.17	101.20	99.62	98.99	99.88	100.29	100.62

Table 1 (continued)

Sample ID	Volcanic rocks																
	Rhyolite									Rhyolitic tuff							
	Rhy01	Rhy02	13-C-17	13-C-44	Rhy03	Rhy04	Rhy05	Chog Rhy	Esf Rhy	Tuff-01	Tuff-02	Tuff-03	Tuff-04	Tuff-05	Tuff-06	Tuff-07	Tuff-08
FeO[a]	1.55	1.84	2.37	2.30	2.83	2.59	1.94	1.57	0.97	0.48	0.73	2.30	0.90	1.35	2.44	2.56	2.81
Rb (ppm)	161.20	152.60	125.80	171.96						48.90	162.90	179.90					
Ba	668.90	550.50	2050.02	4348.87						612.90	550.50	2888.50					
Th	9.40	17.70	10.19	16.31						21.10	7.90	16.00					
U	4.40	6.90	0.80	4.21						4.90	3.30	2.90					
Nb	3.75	3.75	3.75	3.75						7.00	2.90	5.60					
Ta	1.10	1.10	1.10	1.27						nd	nd	nd					
La	91.40	118.80	32.76	95.73						23.50	31.50	39.30					
Ce	37.10	47.80	63.72	193.80						52.50	61.50	84.30					
Pr	4.10	4.20	7.14	18.18						5.60	5.20	7.80					
Sr	62.50	39.60	96.43	68.69						47.50	32.40	64.80					
Nd	15.20	14.50	26.17	57.85						19.40	18.70	27.80					
Zr	173.70	159.10	99.09	307.01						189.30	144.90	159.00					
Hf	3.10	3.10	3.09	7.31						nd	nd	nd					
Sm	2.50	2.90	3.75	8.58						3.10	2.80	5.30					
Eu	0.40	0.60	1.97	5.37						0.60	0.70	1.80					
Ti	14,500	14,500	1386	1416						0.14	0.08	0.11					
Gd	3.50	2.80	3.67	8.97						2.30	2.20	5.60					
Tb	0.50	0.50	0.55	1.06						0.30	0.30	1.10					
Ho	0.50	0.70	0.70	1.19						0.20	0.30	1.30					
Er	1.60	2.10	1.89	3.73						1.00	0.90	3.90					
Yb	1.80	2.40	3.75	3.75						1.40	1.80	3.80					
Lu	0.40	0.40	0.53	1.05						0.20	0.30	0.60					

nd no detection

[a]Chadormalu granitic intrusion, which is a local name for the Zarigan intrusion near the Chadormalu IOA deposit

Table 2 Geochemical analysis of apatites from the Bafq-Saghand metallogenic belt

Deposit	Esfordi						Choghart			Sechahun		Chadormalu			
sample	Ap.C.1	Ap.C.2	Ap.C.3	Ap.C.4	Ap.C.5	Ap.C.6	Ap.C.7	Ap.C.8	Ap.C.9	Ap.C.10	Ap.C.11	Ap.C.12	Ap.C.13	Ap.C.14	Ap.C.15
P (wt.%)	30.33	28.26	30.61	31.44	28.63	30.61	28.34	27.83	29.34	28.95	32.20	27.97	28.54	27.80	28.26
Ca (wt.%)	39	38	38	39	39	39	39	38	38	39	38	38	39	38	38
Si	555	2156	864	2262	592	1095	1662	762	1630	654	1212	691	2167	1785	864
Y	855	859	875	752	870	830	1410	860	1363	825	760	809	787	1325	743
Mg	185	164	51	263	299	75	503	82	468	114	129	253	172	488	299
Mn	112.50	67.21	78.99	85.21	160.84	86.87	188.00	83.25	177.00	90.05	110.50	141.30	70.55	185.00	84.28
Sr	235.21	270.12	165.00	200.20	290.88	175.20	365.00	180.50	351.00	195.90	185.00	251.70	247.20	335.00	165.30
Na	2744	469	1828	531	2875	876	2627	2130	3765	1836	475	2317	373	2799	531
La	1037	5470	439	801	1525	488	2771	592	2719	756	564	1246	2869	2003	488
Ce	2848	11,493	1516	2505	3910	1793	6495	1824	6718	2250	1878	3223	6487	4975	1824
Pr	303	1089	202	270	387	224	647	228	658	259	244	333	622	495	259
Nd	1117	3447	858	1058	1359	953	2216	933	2200	1010	966	1190	2145	1723	1190
Sm	185.10	382.50	176.00	185.00	205.55	178.20	122.89	175.00	330.00	178.00	179.76	191.00	275.20	265.20	271.23
Eu	14.01	19.85	11.02	12.85	19.49	10.46	32.91	12.01	31.98	11.25	11.05	16.15	17.00	27.31	10.55
Gd	171.20	272.20	166.80	167.90	185.01	175.10	291.05	175.00	284.00	165.90	169.02	175.00	213.50	250.05	175.00
Tb	21.46	28.32	21.55	20.58	23.86	22.34	37.87	22.48	36.51	21.16	20.98	21.98	23.83	33.31	20.98
Dy	129	147	129	118	139	130	223	134	218	129	121	130	129	200	218
Ho	25.13	26.42	24.92	22.28	27.22	24.91	43.81	26.08	42.25	24.37	23.04	25.21	23.50	40.36	26.08
Er	64.28	63.30	65.06	56.78	69.90	65.70	117.00	67.65	113.00	64.33	59.44	64.06	57.56	107.00	117.00
Tm	7.76	7.15	8.26	6.73	8.63	8.10	14.65	8.42	13.97	7.52	6.85	7.49	6.54	13.50	6.73
Yb	41.90	36.63	43.76	35.89	47.83	43.85	82.20	44.98	79.30	41.36	37.92	42.62	34.94	74.97	36.63
Lu	5.04	4.48	5.25	4.19	5.72	5.04	9.80	5.38	9.51	4.99	4.49	5.16	4.05	9.08	5.04
LREE	5490	21,882	3191	4819	7387	3636	12,252	3752	12,625	4453	3832	6183	12,398	9461	4032
TREE	5970	22,487	3667	5264	7913	4122	13,104	4248	13,454	4923	4286	6671	12,908	10,217	4648
Eu/Eu*	0.12	0.09	0.10	0.11	0.15	0.09	0.26	0.10	0.16	0.10	0.10	0.13	0.10	0.16	0.07
F	0.75	0.61	0.73	0.86	0.68	0.70	0.56	0.74	0.70	0.73	0.61	0.68	0.71	0.69	0.74
Cl	0.02	0.09	0.08	0.10	0.09	0.09	0.08	0.02	0.09	0.07	0.03	0.08	0.11	0.03	0.02

**Eu is the chondrite-normalized Eu value and Eu* is the average of the chondrite-normalized Sm and Gd concentrations

Table 3 Analytical results from magnetite in iron oxide-apatite deposits of the Bafq-Saghand metallogenic belt

Deposit	Se-chahun							
wt.%	S-M-1	S-M-2	S-M-3	S-M-4	S-M-5	S-M-6	S-M-7	S-M-8
SiO_2	0.04	0.04	< 0.04	< 0.04	< 0.04	0.06	0.05	< 0.04
TiO_2	1.17	0.42	2.52	0.21	1.17	0.41	1.81	1.35
Al_2O_3	1.15	0.24	0.83	0.30	8.20	0.10	0.40	0.60
Cr_2O_3	0.01		0.01		0.02		0.01	0.01
V_2O_5	0.44	0.41	0.40	0.40	0.45	0.44	0.40	0.42
MgO	0.17	0.16	0.18	0.19	0.20	0.18	0.19	0.25
CaO	0.90	< 0.02	1.72	< 0.02	2.46	0.02	2.74	3.96
MnO	0.07	0.07	0.08	0.08	0.08	0.05	0.06	0.05
Fe_2O_3	67.90	67.90	68.00	67.80	67.50	67.40	67.00	67.30
FeO	31.20	31.30	32.00	30.90	31.50	31.30	30.90	31.00
NiO	0.02	0.01	0.02	0.01	0.01	0.02	0.02	0.02
Na_2O	0.08	0.08	0.03	0.14	2.43	0.03	0.02	0.14
K_2O	0.12	0.12	0.02	0.02	1.73	0.02	0.02	0.02
Fe	47.49	47.49	47.56	47.42	47.21	47.14	46.86	47.07
ppm								
Ti	7014.15	2517.90	15,107.40	1258.95	7014.15	2457.95	10,850.95	8093.25
Al	6085.00	1269.91	4391.78	1587.39		529.13	2116.52	3174.78
Cr	22.55		26.74		61.45		21.25	22.64
V	1826.00	2156.00	2838.00	2355.00	1673.00	1894.00	2689.00	2050.00
Ca	6432.21		12,292.67		17,581.37	142.94	19,582.51	28,301.72
Mn	542.10	542.10	619.54	619.54	619.54	387.22	464.66	387.22
Mg	1025.39	965.07	1085.71	1146.02	1206.34	1085.71	1146.02	1507.93
Ni	119.50	78.58	147.80	78.58	97.10	157.16	188.90	150.10
Ge	12.90	10.70	12.60	11.30	11.80	12.10	11.80	10.80
Co	17.60	100.00	34.60	100.00	45.70	100.00	48.80	39.20
Deposit	Se-chahun							
wt.%	S-M-9	S-M-10	S-M-11	S-M-12	S-M-13	S-M-14	S-M-15	S-M-16
SiO_2	0.06	< 0.04	< 0.04	< 0.04	< 0.04	< 0.04	< 0.04	< 0.04
TiO_2	0.98	1.80	2.29	0.39	2.00	0.91	0.22	2.25
Al_2O_3	0.79	0.47	0.49	0.26	0.40	0.34	0.39	0.38
Cr_2O_3	0.01	0.01	0.01		0.01	0.01		0.00
V_2O_5	0.44	0.41	0.44	0.42	4.00	0.45	0.42	0.44
MgO	0.22	0.18	0.15	0.22	0.21	0.17	0.18	0.19
CaO	9.61	3.12	1.58	< 0.02	1.13	1.89	< 0.02	0.43

Table 3 (continued)

Deposit	Se-chahun							
wt.%	S-M-9	S-M-10	S-M-11	S-M-12	S-M-13	S-M-14	S-M-15	S-M-16
MnO	0.08	0.07	0.13	0.14	0.10	0.12	< 0.04	< 0.04
Fe_2O_3	68.10	68.05	68.20	67.40	67.50	68.00	67.00	67.10
FeO	31.20	31.00	32.10	31.00	31.50	32.00	31.00	30.80
NiO	0.02	0.02	0.02	0.03	0.02	0.03	0.03	0.03
Na_2O	0.02	0.04	0.02	2.43	0.04	0.03	0.02	0.01
K_2O	0.08	0.02	0.02	1.73	0.02	0.02	0.02	0.02
Fe	47.63	47.60	47.70	47.14	47.21	47.56	46.86	46.93
ppm								
Ti	5875.10	10,791.00	13,728.55	2338.05	11,990.00	5455.45	1318.90	13,488.75
Al	4180.13	2486.91	2592.74	1375.74	2116.52	1799.04	2063.61	2010.69
Cr	27.14	23.99	29.26		26.15	23.63		19.77
V	2423.00	1760.00	2283.00	1984.00	2415.00	2109.00	2125.00	2313.00
Ca	68,681.71	22,298.33	11,292.10		8076.00	13,507.64		3073.17
Mn	619.54	542.10	1006.76	1084.20	774.43	929.32		
Mg	1326.97	1085.71	904.76	1326.97	1266.66	1025.39	1085.71	1146.02
Ni	128.60	136.20	160.20	235.73	189.40	247.10	235.73	230.80
Ge	10.50	10.70	11.50	11.30	12.20	12.40	11.64	10.30
Co	25.10	48.90	48.50	93.50	73.40	93.50	52.80	96.90
Deposit	Chadormalu							
wt.%	lu-M-1	lu-M-2	lu-M-3	lu-M-4	lu-M-5	lu-M-6	lu-M-7	
SiO_2	0.06	< 0.04	< 0.04	0.42	0.02	0.13	0.05	
TiO_2	2.28	1.05	1.42	1.56	0.72	0.50	1.12	
Al_2O_3	0.34	0.26	0.30	0.30	0.09	0.24	0.07	
Cr_2O_3	0.00	0.00	0.00	0.00	0.00	0.00	0.00	
V_2O_5	0.41	0.40	0.42	0.44	0.53	0.21	0.57	
MgO	0.22	0.17	0.20	0.20	1.15	1.52	1.00	
CaO	1.33	6.10	10.66	8.52	1.24	1.66	2.57	
MnO	< 0.04	0.14	0.12	< 0.04	0.41	0.23	0.17	
Fe_2O_3	67.20	67.25	67.00	68.00	68.21	67.05	65.87	
FeO	31.00	31.30	31.00	32.00	27.61	28.04	28.94	
NiO	0.03	0.03	0.03	0.03	0.01	0.00	0.01	
Na_2O	0.05	0.06	0.04	0.04	0.09	0.09	0.02	
K_2O	0.02	0.02	0.02	0.02	0.14	0.12	0.03	
Fe	47.00	47.04	46.86	47.56	47.71	46.90	46.07	

Table 3 (continued)

Deposit	Chadormalu						
wt.%	lu-M-1	lu-M-2	lu-M-3	lu-M-4	lu-M-5	lu-M-6	lu-M-7
ppm							
Ti	13,668.60	6294.75	8512.90	9352.20	4316.40	2997.50	6714.40
Al	1799.04	1375.74	1587.39	1587.39	476.22	1269.91	370.39
Cr	10.35	11.03	9.86	15.71	14.81	13.17	9.25
V	2390.00	2014.00	1890.00	2022.00	3602.73	1427.50	3874.63
Ca	9505.38	43,596.09	76,185.95	60,891.59	8862.16	11,863.85	18,367.53
Mn		1084.20	929.32		3175.16	1781.19	1316.53
Mg	1326.97	1025.39	1206.34	1206.34	6936.46	9168.18	6031.70
Ni	248.00	221.70	201.40	201.80	107.50	35.50	82.40
Ge	12.10	11.47	11.30	12.90	12.05	12.36	11.01
Co	98.80	52.80	76.30	69.80	115.50	97.30	116.90
Deposit	Choghart							
wt.%	rt-M-1	rt-M-2	rt-M-3	rt-M-4	rt-M-5	rt-M-6	rt-M-7	rt-M-8
SiO_2	0.06	0.25	0.09	0.01	0.04	0.08	0.09	0.11
TiO_2	0.69	0.63	0.54	0.57	0.69	0.78	1.00	1.02
Al_2O_3	0.11	0.15	0.12	0.12	0.11	0.08	0.10	0.10
Cr_2O_3	0.00	0.00	0.00	0.00	0.00	0.00	0.00	0.00
V_2O_5	0.80	0.23	0.41	0.46	0.29	0.32	0.26	0.12
MgO	1.50	2.20	0.87	1.16	1.12	0.74	0.91	0.63
CaO	1.98	2.09	2.86	2.37	2.69	4.15	1.25	2.43
MnO	0.22	0.23	0.12	0.04	0.16	0.22	0.11	0.10
Fe_2O_3	64.65	65.80	66.54	65.51	66.20	66.10	66.25	66.00
FeO	29.33	28.57	28.64	29.00	28.10	26.80	29.37	29.50
NiO	0.01	0.02	0.01	0.01	0.02	0.02	0.02	0.01
Na_2O	0.13	2.55	0.04	0.02	0.13	0.03	0.05	0.01
K_2O	0.02	1.55	0.03	0.01	0.02	0.08	0.03	0.02
Fe	45.22	46.02	46.54	45.82	46.30	46.23	46.34	46.16
ppm								
Ti	4136.55	3776.85	3237.30	3417.15	4136.55	4676.10	5995.00	6114.90
Al	582.04	793.70	634.96	634.96	582.04	423.30	529.13	529.13
Cr	10.65	14.98	11.35	5.97	15.00	8.84	10.65	12.00
V	5438.08	1563.45	2787.02	3126.90	1971.30	2175.23	1767.38	815.71
Ca	14,150.86	14,937.02	20,440.13	16,938.15	19,225.16	29,659.64	8933.63	17,366.97
Mn	1703.75	1781.19	929.32	309.77	1239.09	1703.75	851.87	774.43

Table 3 (continued)

Deposit	Choghart								
wt.%	rt-M-1	rt-M-2	rt-M-3	rt-M-4	rt-M-5	rt-M-6	rt-M-7	rt-M-8	
Mg	9047.55	13,269.74	5247.58	6996.77	6755.50	4463.46	5488.85	3799.97	
Ni	62.70	150.10	100.30	100.90	177.80	140.20	135.70	105.00	
Ge	10.40	11.64	12.01	11.88	11.30	10.60	10.55	11.64	
Co	72.10	122.60	118.80	95.50	127.20	150.00	130.00	100.70	
Deposit	Choghart								
wt.%	rt-M-9	rt-M-10	rt-M-11	rt-M-12	rt-M-13	rt-M-14	rt-M-15	rt-M-16	rt-M-17
SiO_2	0.13	0.07	0.03	0.17	0.11	0.11	0.16	0.13	0.07
TiO_2	0.59	0.25	1.13	0.98	0.68	0.51	0.47	0.55	0.70
Al_2O_3	0.06	0.11	0.14	0.34	0.28	0.12	0.15	0.12	0.14
Cr_2O_3	0.00	0.00	0.00	0.00	0.00	0.00	0.00	0.00	0.00
V_2O_5	0.48	0.39	0.48	0.16	0.20	0.44	0.08	0.64	0.53
MgO	0.85	1.05	1.30	1.06	0.46	1.39	1.67	0.63	1.09
CaO	2.27	1.45	2.56	2.72	2.04	3.72	2.95	2.16	3.07
MnO	0.19	0.27	0.18	0.31	0.31	0.09	0.09	0.22	0.17
Fe_2O_3	66.40	66.00	66.22	65.86	66.24	65.40	66.30	68.62	65.48
FeO	28.70	30.20	28.42	28.27	28.72	28.00	27.90	26.81	28.29
NiO	0.01	0.01	0.02	0.01	0.00	0.01	0.02	0.02	0.01
Na_2O	2.64	0.04	0.03	0.04	0.04	0.06	0.05	0.02	0.01
K_2O	1.50	0.02	0.02	0.03	0.03	0.03	0.03	0.03	0.02
Fe	46.44	46.16	46.32	46.07	46.33	45.74	46.37	48.00	45.80
ppm									
Ti	3537.05	1498.75	6774.35	5875.10	4076.60	3057.45	2817.65	3297.25	4196.50
Al	317.48	582.04	740.78	1799.04	1481.56	634.96	793.70	634.96	740.78
Cr	8.37	10.94	7.78	9.60	17.38	8.72	8.37	12.06	5.92
V	3262.85	2651.06	3262.85	1087.62	1359.52	2990.94	543.81	4350.46	3602.73
Ca	16,223.46	10,363.01	18,296.06	19,439.57	14,579.68	26,586.47	21,083.36	15,437.30	21,940.98
Mn	1471.42	2090.96	1393.97	2400.73	2400.73	696.99	696.99	1703.75	1316.53
Mg	5126.95	6333.29	7841.21	6393.60	2774.58	8384.06	10,072.94	3799.97	6574.55
Ni	114.80	61.78	150.20	73.60	37.40	85.90	170.00	125.40	114.80
Ge	13.10	11.40	12.00	11.80	12.35	13.01	10.44	10.52	11.55
Co	110.10	90.50	130.70	114.40	105.20	180.60	139.10	136.10	119.50

Table 3 (continued)

wt.%	Esfordi									
	E-M-1	E-M-2	E-M-3	E-M-4	E-M-5	E-M-6	E-M-7	E-M-8	E-M-9	E-M-10
SiO_2			0.06	0.86	0.05	0.04	0.02		0.03	0.06
TiO_2	0.30	0.05	0.09	0.09	0.04	0.07	0.77	0.08	0.02	0.16
Al_2O_3	0.04			0.08				0.02		
Cr_2O_3	0.02	0.02					0.02	0.02	0.02	0.02
V_2O_5	0.33	0.29	0.22	0.25	0.26	0.23	0.36	0.33	0.34	0.36
MgO				0.36					0.03	
CaO	0.02	0.01	0.01	0.20	0.01	0.06	0.03	0.00	0.03	
MnO				0.03	0.02	0.04	0.02		0.01	
Fe_2O_3	67.61	68.62	67.89	66.67	68.15	68.85	66.64	68.04	68.04	67.88
FeO	31.79	31.65	31.33	32.00	31.45	31.67	32.25	31.68	31.59	31.95
NiO	0.10	0.09	0.11	0.04	0.10	0.06	0.11	0.04		
Na_2O		0.07		0.11		0.04	0.02	0.04	0.04	
K_2O										
Fe	47.29	47.99	47.49	46.63	47.66	48.16	46.61	47.59	47.59	47.48
ppm										
Ti	1816.49	275.77	545.55	515.57	227.81	443.63	4598.17	503.58	143.88	959.20
Al	211.65			428.60				95.24		
Cr	72.08	84.09					80.09	72.08	72.08	84.09
V	1865.37	1607.69	1204.37	1417.23	1445.24	1271.59	1994.21	1854.16	1921.38	1988.60
Ca	164.38	64.32	50.03	1422.23	57.18	421.67	200.11	21.44	242.99	
Mn				240.07	170.37	309.77	139.40		92.93	
Mg				2195.54					150.79	
Ni	754.35	691.49	832.93	337.89	777.92	471.47	864.36	306.45		
Ge	11.65	10.70	11.64	11.30	10.80	12.10	11.80	12.20	10.50	11.45
Co										

wt.%	Esfordi									
	E-M-11	E-M-12	E-M-13	E-M-14	E-M-15	E-M-16	E-M-17	E-M-18	E-M-19	E-M-20
SiO_2	0.05	0.04			0.36	0.11	0.04	0.02	0.06	0.04
TiO_2	0.04	0.20	0.65	0.03	0.10	0.03	0.03	0.05		0.20
Al_2O_3	0.02		0.09					0.02	0.03	
Cr_2O_3		0.02	0.03							0.02
V_2O_5	0.29	0.29	0.06	0.61	0.32	0.25	0.30	0.28	0.22	0.29
MgO			0.00	0.02	0.12	0.03		0.02		
CaO	0.05	0.04	0.03	0.11	0.07	0.00	0.52	0.00	0.02	0.04

Table 3 (continued)

wt.%	Esfordi									
	E-M-11	E-M-12	E-M-13	E-M-14	E-M-15	E-M-16	E-M-17	E-M-18	E-M-19	E-M-20
MnO			0.07			0.01	0.03	0.04		
Fe_2O_3	68.56	67.16	67.12	67.22	66.45	67.83	67.71	67.60	68.18	67.16
FeO	31.76	31.42	31.52	31.81	31.54	31.45	30.78	31.23	31.39	31.42
NiO	0.04	0.03						0.07	0.05	0.03
Na_2O			0.03						0.03	
K_2O	0.03		0.04					0.01		0.01
Fe	47.96	46.98	46.95	47.01	46.48	47.44	47.36	47.28	47.69	46.98
ppm										
Ti	209.83	1222.98	3890.76	197.84	599.50	197.84	197.84	299.75		1222.98
Al	116.41		486.80					84.66	153.45	
Cr		72.08	136.15							72.08
V	1646.90	1646.90	336.10	3400.23	1798.15	1400.43	1697.32	1590.88	1249.18	1646.90
Ca	350.20	293.02	214.41	800.45	500.28		3702.09		128.64	293.02
Mn			526.61			100.68	201.35	309.77		
Mg				102.54	699.68	199.05		96.51		
Ni	275.02	251.45						526.47	361.46	251.45
Ge	11.50	11.30	10.70	12.40	12.60	10.30	10.40	11.80	12.60	10.70
Co										

wt.%	Esfordi										
	E-M-21	E-M-22	E-M-23	E-M-24	E-M-25	E-M-26	E-M-27	E-M-28	E-M-29	E-M-30	E-M-31
SiO_2	0.02		0.04			0.04	0.01	0.07	0.02	0.02	0.05
TiO_2	0.02	0.36	0.32	0.35	0.30	0.09		0.26		0.02	0.05
Al_2O_3		0.16	0.16	0.14	0.14	0.22					0.01
Cr_2O_3	0.03	0.03				0.06	0.02	0.02	0.04	0.03	
V_2O_5	0.09	0.42	0.41	0.26	0.45	0.05		0.22	0.29	0.09	0.04
MgO	0.02			0.05	0.05					0.02	0.58
CaO	0.05		0.02		0.00	0.23	0.06	0.08	0.16	0.05	0.18
MnO		0.03				0.01	0.02		0.02		0.02
Fe_2O_3	67.96	66.54	67.03	67.31	67.00	68.17	68.63	68.07	67.24	67.96	68.88
FeO	30.75	31.79	32.03	31.61	31.89	30.95	30.83	31.74	30.91	30.75	30.03
NiO	0.06	0.05	0.03	0.03	0.03			0.02		0.06	
Na_2O		0.04	0.01	0.01	0.01				0.02		0.07
K_2O	0.01				0.00	0.01	0.02	0.02			0.05
Fe	47.53	46.54	46.88	47.08	46.86	47.68	48.00	47.61	47.03	47.53	48.18

Table 3 (continued)

wt.%	Esfordi										
	E-M-21	E-M-22	E-M-23	E-M-24	E-M-25	E-M-26	E-M-27	E-M-28	E-M-29	E-M-30	E-M-31
ppm											
Ti	101.92	2152.21	1936.39	2098.25	1798.50	563.53		1564.70		95.92	299.75
Al		867.77	857.19	714.33	714.33	1164.09					52.91
Cr	120.13	104.11				220.24	96.11	96.11	172.19	120.13	
V	498.55	2324.71	2291.10	1478.85	2509.56	302.49		1209.97	1635.70	498.55	207.26
Ca	335.90		107.20		28.59	1629.49	414.52	557.46	1157.80	335.90	1250.71
Mn		263.31				69.70	170.37		147.14		116.16
Mg	108.57			319.68	319.68					108.57	3516.48
Ni	447.89	400.75	220.02	235.73	235.73			165.01		447.89	
Ge	12.60	12.20	11.50	12.90	10.80	9.40	11.20	10.10	10.70	12.10	10.80
Co											

Al_2O_3 (11–21 wt. %), Ba (61–868 ppm), Zr (85–259 ppm), concentrations.

Based on the TAS diagram for igneous rocks ($Na_2O + K_2O$ versus SiO_2) (Middlemost, 1985), the analyzed samples classify as granite, granodiorite, monzonite, syenite, and monzosyenite (Fig. 6a), while rhyolite compositions are dominant in respect to volcanic rocks in the region (cf., Le Bas et al. 1986) (Fig. 6b). Overall two compositional series emerge: a sub-alkaline one versus an alkaline one. Using the AFM diagram, which separates calc-alkaline igneous rocks from tholeiitic rocks (Irvine and Bargar 1971), all of the igneous rocks are of calc-alkaline composition and plot in the right-side corner of the diagram (Fig. 7a, b). When plotting $Na_2O + K_2O + CaO$ versus SiO_2 on a Mali diagram (Fig. 8; Frost and Frost 2008), two groups of plutonic rocks emerge also. The first one is mostly composed of calc-alkaline rocks and includes the Zarigan igneous granitic bodies, and the Chadormalu, Narigan and Ariz intrusions, whereas the second group belongs to the alkaline compositional series and includes, e.g., the Narigan and the Esfordi syenites (Figs. 7, 8). According to Fig. 8, most of the regional volcanic samples fall within the calc-alkaline domain; however, two samples from the Esfordi rhyolites have alkaline affinity. These two samples are from close to the metasomatized ore zone. Considering that the samples are collected from alkaline metasomatized and alkaline bodies, we consider these specific samples, similar to Majidi et al. (2015), to reflect secondary hydrothermal overprint on the Esfordi rhyolites.

Apatite

The analytical results of 15 representative samples of apatite crystals are presented in Table 2. Sr and Y contents of apatites determined in this study range from 165 to 365 ppm and from 743 to 1410 ppm, respectively. Mn and Mg content of apatite samples are 67 to 188 ppm and 51 to 503 ppm, respectively. The most noticeable result of the apatites is high LREE contents that are ranging from 0.3 wt. % up to 2.2 wt. %. The Eu content is 10.5 ppm to 33 ppm and shows a clear negative anomaly ($Eu/Eu^* = 0.07$ to 0.26). The apatite samples also show contents of F and Cl, ranging from 0.6 ppm to 0.9 ppm and from 0.02 ppm to 0.11 ppm, respectively.

Magnetite

Analytical results of 71 magnetite crystal separate samples from iron oxide-apatite deposits within the Bafq-Saghand metallogenic belt are presented in Tables 3 and 4. TiO_2 content of the studied magnetites varies from 0.02 to 2.5 wt. %, and Al_2O_3 values range from 0.01 to 1.15 wt. % with one exception, namely magnetite from the partly metasomatised Se-Chahun deposit that shows an Al_2O_3 content of up to

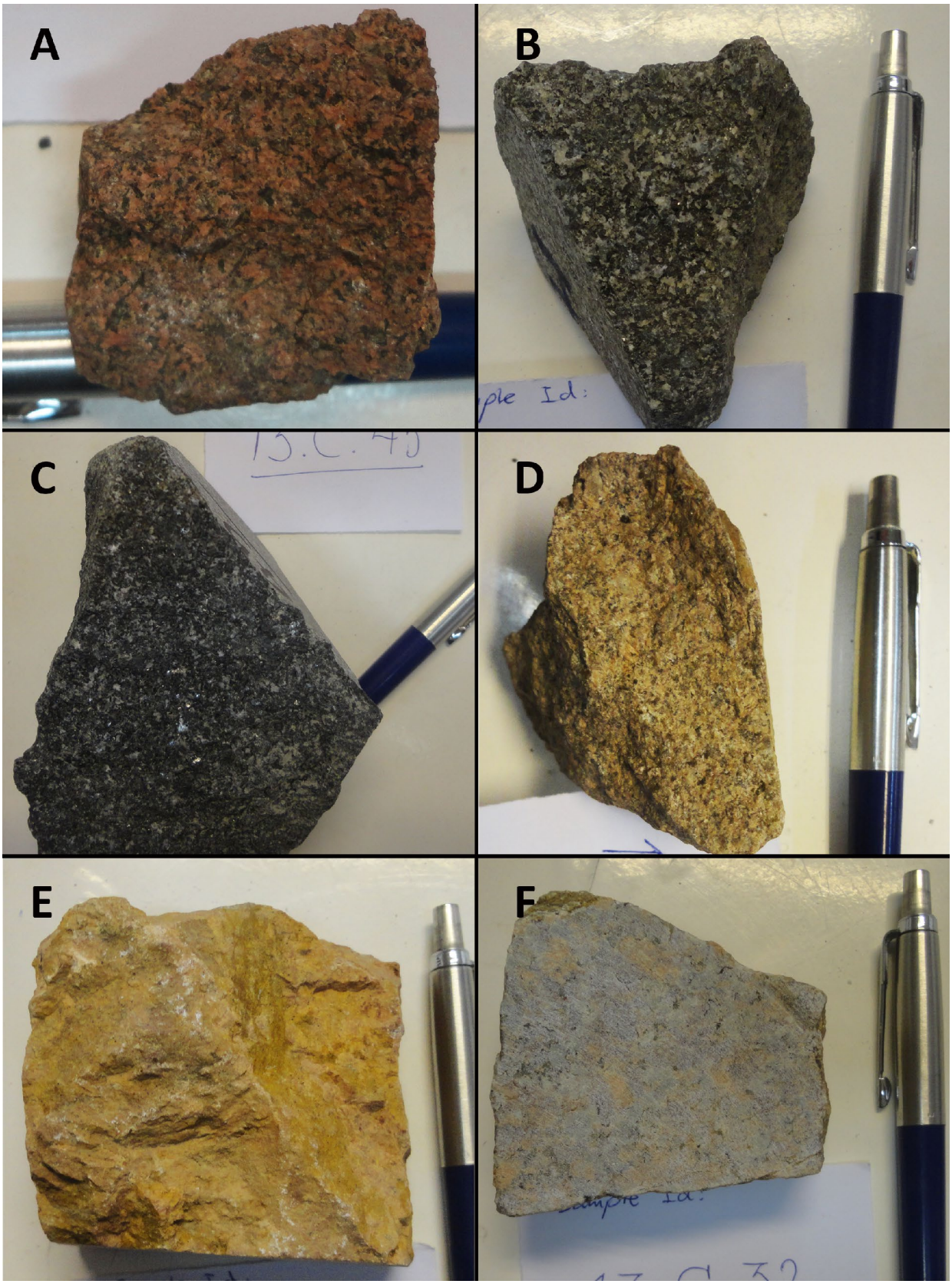

Fig. 5 Representative rock samples of alkaline and calk-alkaline igneous intrusion in the Bafq-Saghand belt. **a** Narigan Syenite. **b** Esfordi Syenite. **c** Esfordi Syenite (more mafic minerals). **d** North Esfordi Syenite (Arash Syenite). **e** Chadormalu Micro-granite. **f** Narigan Granite

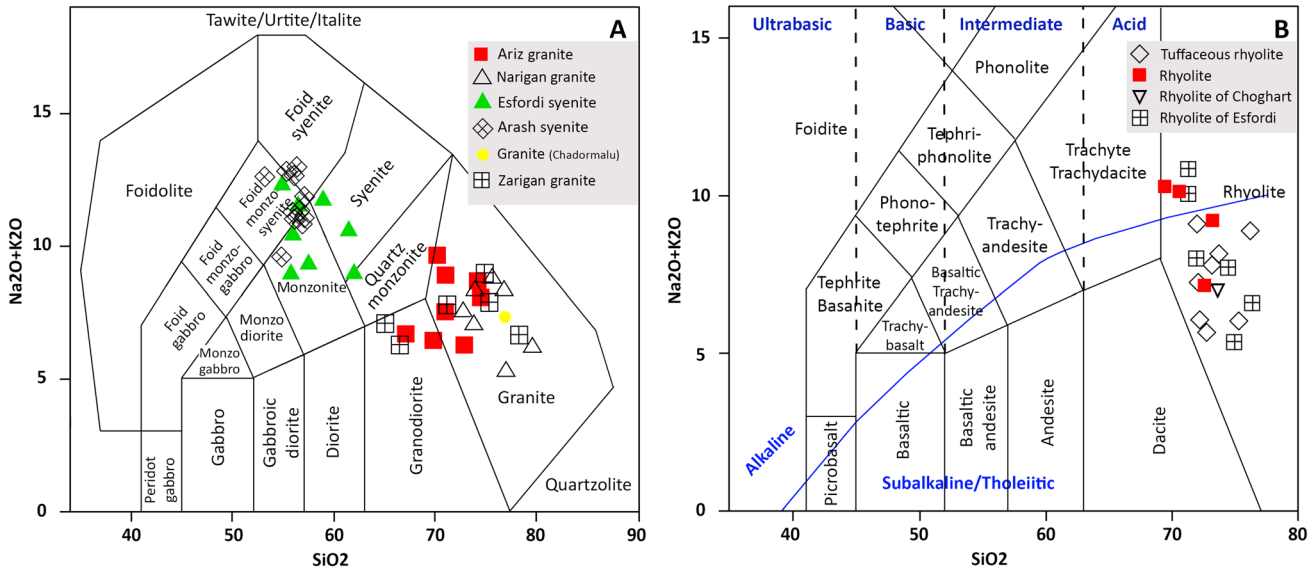

Fig. 6 **a** Classification diagram of Na_2O+K_2O versus SiO_2 (after Middlemost 1985) for intrusive rocks. The petrological composition of the samples is mostly granite, granodiorite, monzonite, syenite, monzosyenite and diorite. **b** Diagram of Na_2O+K_2O versus SiO_2 (after Le Bas et al. 1986) for volcanic rocks. The petrological composition of the samples marks them as predominantly rhyolite

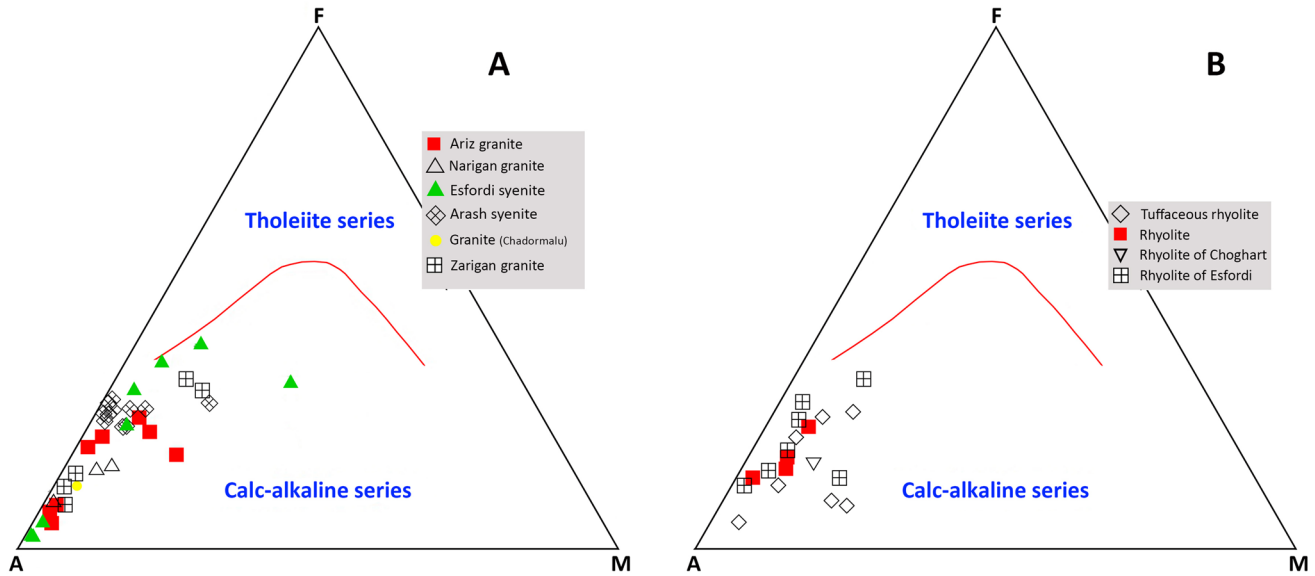

Fig. 7 AFM diagram which separates calc-alkaline igneous rocks from tholeiitic igneous rocks (after Irvine and Bargar 1971). See text for details

8.2 wt. %. In terms of Cr_2O_3 content, the majority of the Bafq-Saghand magnetites are poor (0.002–0.06 wt. %) and *V* content is also low, varying between 0.2 and 0.6 wt. %. Mn values range from 0.01 to 0.31 wt. % and values of other common elements (ppm) are 97–13,270 for Mg, 35–864 for Ni and 17–180 for Co (Table 3).

Oxygen isotope

The $\delta^{18}O$ ratios of most of the collected magnetite samples (16 magnetite samples, Table 5), vary between −0.1 and +2.2 ‰ ($n=14$). Values higher than this range are recorded in a small number of samples from altered

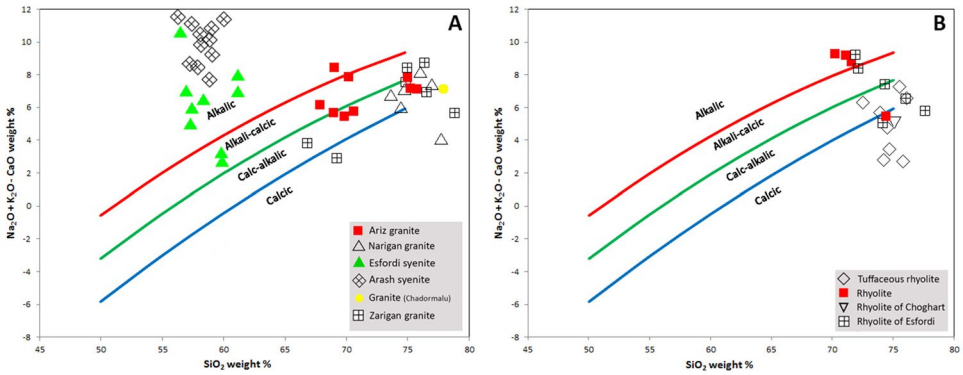

Fig. 8 Mali diagram which plots $Na_2O + K_2O$–CaO versus SiO_2 (Frost and Frost 2008). Two groups of igneous rocks emerge. The first one is composed of calc-alkaline and alkaline-calcic rocks and includes the main granitic intrusions of the study region, whereas the second group is composed of syenitic rocks and belongs to the alkaline compositional series

Table 4 Statistical values of magnetite samples from iron oxide-apatite deposits within the Bafq-Saghand metallogenic belt

Deposit	Esfordi			Sechahun			Chadormalu			Choghart		
wt %	Min	Max	Ave	Min	Max	Ave	Min	Max	Ave	Min	Max	Ave
Ti	0.01	0.46	0.10	0.13	1.51	0.75	0.30	1.37	0.74	0.15	0.68	0.42
Al	0.01	0.12	0.05	0.05	0.61	0.25	0.04	0.18	0.12	0.03	0.18	0.07
Cr	0.01	0.02	0.01	0.00	0.01	0.00	0.00	0.00	0.00	0.00	0.00	0.00
V	0.02	0.34	0.15	0.17	0.28	0.22	0.14	0.39	0.25	0.05	0.54	0.25
Ti + Al	0.01	0.58	0.15	0.18	2.12	1.00	0.34	1.55	0.86	0.18	0.86	0.49
ppm												
Mn	69.70	527	204	387	1084	653	929	3175	1657	310	2401	1380
Mg	96.51	3516	711	905	1508	1146	1025	9168	3843	2775	13,270	6610
Ni	165.01	864.36	442.79	78.58	247.10	161.34	35.50	248.00	156.90	37.40	177.80	112.15
Co	nd	nd	nd	17.6	100	63.66	52.80	116.90	89.63	72.10	180.60	120.18

nd no detection

Table 5 $\delta^{18}O$ isotopic results of the Bafq-Saghand iron oxide (magnetite) deposits

Sample Id	Deposit	Mineral type	δ18O ‰ SMOW	Description
O 15.01	Esfordi	Magnetite	1.20	Massive brecciated magnetite–apatite
O 15.02	Esfordi	Magnetite	− 0.10	Detrital magnetite
O 15.03	Chadormalu	Magnetite	2.20	Magnetite in brecciated type apatite
O 15.04	Chadormalu	Magnetite	0.10	Massive brecciated magnetite
O 15.05	Chadormalu	Magnetite	1.70	Massive magnetite
O 15.06	Chadormalu	Magnetite	1.40	Main apatite ore
O 15.07	Chadormalu	Magnetite	− 0.10	Massive magnetite
O 15.08	Esfordi	Magnetite	6.76	Magnetite in brecciated altered tuff of the apatite ore
O 15.09	Choghart	Magnetite	0.30	Massive magnetite
O 15.10	Choghart	Magnetite	2.10	Magnetite sublayers in tuffaceous sandstone
O 15.11	Choghart	Magnetite	1.60	Brecciated apatite, rim of Fe-oxide core
O 15.12	Choghart	Magnetite	0.00	Disseminated magnetite in rhyolite
O 15.13	Sechahun	Magnetite	1.70	Fe-oxide-jaspilite layer
O 15.14	Esfordi	Magnetite	4.73	Magnetite in brecciated apatite ore
O 15.15	Sechahun	Magnetite	1.40	Main apatite ore
O 15.16	Sechahun	Magnetite	− 0.10	Massive magnetite
O 15.17	Esfordi	Magnetite	4.80	Magnetite in brecciated apatite ore
O 15.18	Sechahun	Magnetite	1.50	Massive magnetite
O 15.19	Sechahun	Magnetite	2.00	Magnetite in brecciated type apatite
O 15.20	Esfordi	Magnetite	6.50	Magnetite in brecciated altered tuff of the apatite ore

brecciated tuff-derived magnetite samples (+4.7 to +6.8 ‰; $n=4$).

U–Pb dating

A total of 22 zircon grains from alkaline syenitic samples were analyzed for U–Pb zircon geochronology (Table 6; Fig. 9). Zircon grains from the syenite samples are dominated by one major age populations of 469 to 411 Ma with average of 437. 25 ± 5 Ma.

Discussion

Geochemistry of the ore deposits

Apatite geochemistry

Crystallization of phosphates is an important process toward the concentration of elements such as U, Th, Sr, Y and REEs (Ayers and Watson 1993; Roeder et al. 1987; Toplis and Dingwell 1996). Thus, geochemical investigations of the Bafq-Saghand phosphate bearing minerals (Fig. 10), in particular apatite, can provide insights into geological evolutions (Sha and Chappell 1999; Belousova 2000; Belousova et al. 2001, 2002). Considering the F-OH-Cl content of the apatite samples, the determined values are scattered within the hydroxyl-fluorapatite domain (Fig. 11), and F/OH ratios are higher than 2. These results are consistent with previus studies on the Bafq-Saghand belt's iron-apatite deposits (Daliran 2002; Moore and Modabberi 2003, Torab and Lehmann 2007; Bonyadi et al. 2011; Heidarian et al. 2018) and with data from Abagong, in China (Yang et al. 2013); Avnik, in Turkey (Chai et al. 2014); Grängesberg, in Sweden (Jonsson et al. 2013), and Kiruna in Sweden (Harlov et al. 2002). Specifically, the apatite samples in this study are enriched with Si, Na, Y and sometimes Cl due to sodic alteration (Bonyadi et al. 2011). Sr (165–365 ppm) and Y (743–1410 ppm) contents of the studied apatites are different from carbonatitic apatite (Table 2) since Sr contents of carbonatitic apatites are > 2500 ppm and the Y contents are < 400 ppm (Belousova et al. 2002). Considering Sr–Y (Fig. 12a) and Sr-Mn contents (Fig. 12b), the studied apatites show values that are more typical forapatites associated with mafic igneous rocks and with Kiruna-type deposits (e.g., Belousova et al. 2002; Frietsch and Perdahl 1995). Hence, Torab and Lehman (2007) claimed that the dioritic igneous bodies in the region are of high importance toward generating the iron oxide-apatite deposits. The accumulation grade of REEs in apatite in the Bafq-Saghand belt is ranging between 0.36 and 2.25 percent in LREEs (Table 2). Patterns in a REE spider diagram normalized to chondrite indicate high depletion of Eu (Eu/Eu* = 0.07–0.26) relative to the other REE as well as a contrast between LREEs and HREEs (Fig. 12d). The depletion of Eu is likely a result of magmatic processes and low oxygen fugacity (so that Eu^{2+} can substitute for Ca^{2+}). Hence, during fractional crystallization, Eu^{2+} is substituted for Ca^{2+} in, e.g., plagioclase and then extracted from the magma, leading to consequent depletion of Eu in the melt (Sverjensky 1984; Wood 1990a, b). In carbonatitic apatites, depletion of Eu is usually not observed or negligible, which is not in line with our studied examples. Fractionation of LREE and HREE is small and follows a linear trend (Belousova et al. 2002). Considering the REE patterns in the studied apatites (Fig. 12d), they are similar to those from I-type granites (Sha and Chappell 1999). According to the Y vs Eu/Eu* diagram (Belousova et al. 2002), the studied samples show once more similarities with the apatites from Kiruna-type deposits, mafic rocks and granitoids (Fig. 12c), which is supported by the Sr–Y and Sr–Mn patterns (Fig. 12). This points towards a primary magmatic origin of the Bafq-Saghand iron oxide-apatite ores and supports an association with the calc-alkaline magmatic suite in the region.

Magnetite geochemistry

Magnetite can form in different physio–chemical environments, including silicate magma, carbonatite magmas, and from low temperature hydrothermal fluids. These different conditions can result in variable concentrations of REE in magnetite (Dupuis and Beaudoin 2011; Nadoll et al. 2014). The differences in trace elements (Ti, V, Cr, Ni, etc.) and some REEs during magnetite mineralization are believed to be systematic (Dare et al. 2014) and are dominantly governed by different partition behavior of trace elements in distinct magnetite forming environments. Considering this geochemical behavior of REEs, several studies have exploited this concept to differentiate between distinct formation processes and mineralization systems (Grigsby 1990; Reguir et al. 2008; Pecoits et al. 2009; Rusk et al. 2010; Dupuis and Beaudoin 2011; Dare et al. 2012; Angerer et al. 2012; Nadoll et al. 2012; Dare et al. 2014; Nadoll et al. 2014; Chen et al. 2015; Ovalle et al. 2018; Sun et al. 2019).

The full magnetite data in our study scatter across the domains for felsic magma (Sawyer 2010), I-type granites (Dare et al. 2014), and hydrothermal magnetites (e.g., Ray and Webster 2007; Dupuis and Beaudoin 2011; Nadoll et al. 2012; Nadoll et al. 2014), but are broadly similar to Kiruna-type iron ore mineralization where the Ti content is typically low (100–1000 ppm), although some exceptional samples show 5000 ppm, and the Al content varies from 200 to 1500 ppm (Nyström and Henriquez 1994). Moreover, the low value of Cr_2O_3 is one of the main geochemical features

Table 6 U–Pb zircon dating results from the Bafq-Saghand alkaline intrusions

Sample	U (ppm)	Th/U	U–Th–Pb ratios								Ages (Ma)						Inferred age (Ma)	1σ
			$^{207}Pb/^{235}U$	1σ	$^{206}Pb/^{238}U$	1σ	$^{207}Pb/^{206}Pb$	1σ	$^{208}Pb/^{232}Th$	1σ	$^{206}Pb/^{238}U$	1σ	$^{207}Pb/^{206}Pb$	1σ	$^{207}Pb/^{235}U$	1σ		
Esfordi syenite																		
13.C.41–1	115	0.36	0.53974	0.01033	0.06731	0.00085	0.05817	0.00055	0.02190	0.00089	420	5	536	19	438	7	420	5
13.C.41–2	195	1.18	0.53081	0.00886	0.06997	0.00086	0.05503	0.00043	0.02143	0.00084	436	5	413	16	432	6	436	5
13.C.41–3	509	1.44	0.55591	0.00799	0.07126	0.00086	0.05659	0.00036	0.02243	0.00091	444	5	476	13	449	5	444	5
13.C.41–4	131	0.65	0.52741	0.00995	0.06627	0.00084	0.05773	0.00054	0.02086	0.00092	414	5	520	18	430	7	414	5
13.C.41–5	320	0.81	0.52819	0.00819	0.06863	0.00084	0.05582	0.00039	0.02205	0.00099	428	5	445	14	431	5	428	5
13.C.41–6	590	1.14	0.54329	0.00792	0.06979	0.00085	0.05647	0.00036	0.02274	0.00107	435	5	471	13	441	5	435	5
13.C.41–7	114	0.54	0.53989	0.01063	0.06581	0.00085	0.05951	0.00059	0.02292	0.00117	411	5	586	19	438	7	411	5
13.C.41–9	60	0.36	0.49873	0.01298	0.06763	0.00093	0.05350	0.00080	0.02723	0.00161	422	6	350	30	411	9	422	6
13.C.41–10	317	0.87	0.54397	0.00890	0.07025	0.00087	0.05617	0.00042	0.02524	0.00155	438	5	459	15	441	6	438	5
13.C.41–11	49	0.38	0.57862	0.01603	0.06852	0.00097	0.06126	0.00099	0.02923	0.00184	427	6	648	31	464	10	427	6
13.C.41–12	553	1.48	0.57091	0.00886	0.07258	0.00089	0.05705	0.00040	0.02631	0.00169	452	5	494	14	459	6	452	5
Narigan syenite																		
13.C.02–02	81	11.03	0.59101	0.01156	0.07147	0.00090	0.05998	0.00059	0.02425	0.00084	445	5	603	19	472	7	445	5
13.C.02–03	917	2.48	0.52690	0.00708	0.07076	0.00083	0.05401	0.00032	0.02624	0.00093	441	5	371	12	430	5	441	5
13.C.02–04	84	14.18	0.54894	0.01412	0.07434	0.00102	0.05356	0.00078	0.02372	0.00087	462	6	353	30	444	9	462	6
13.C.02–05	961	2.36	0.56090	0.00752	0.07119	0.00083	0.05715	0.00033	0.02554	0.00097	443	5	497	12	452	5	443	5
13.C.02–06	39	19.85	0.53685	0.01510	0.07179	0.00098	0.05424	0.00092	0.02350	0.00092	447	6	381	34	436	10	447	6
13.C.02–08	74	14.18	0.60019	0.02628	0.07542	0.00132	0.05772	0.00168	0.02342	0.00100	469	8	519	58	477	17	469	8
13.C.02–09	870	2.84	0.53730	0.00738	0.07129	0.00084	0.05467	0.00033	0.02407	0.00105	444	5	399	12	437	5	444	5
13.C.02–10	677	1.95	0.54821	0.00793	0.06901	0.00082	0.05762	0.00037	0.02292	0.00104	430	5	515	13	444	5	430	5

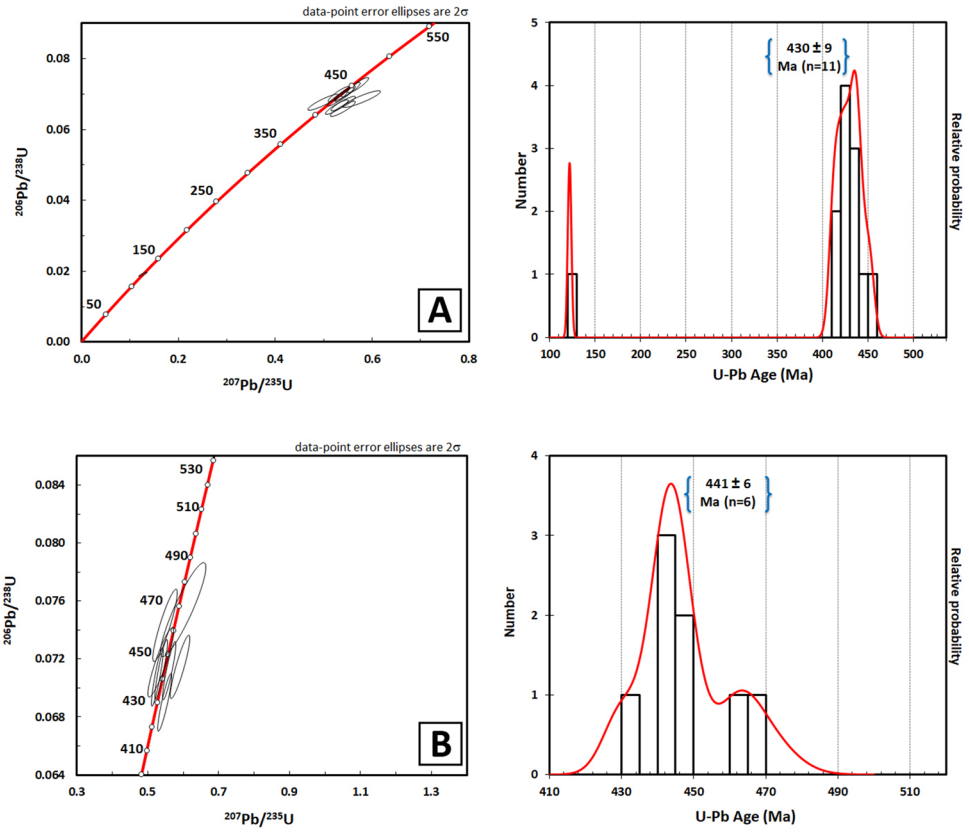

Fig. 9 Zircon U–Pb analysis of zircons from alkaline rocks in the Bafq-Saghand metallogenic belt. **a** Concordia diagram of the Narigan syenite and weighted mean of the Narigan syenite. **b** Concordia diagram of the Esfordi syenite and average weighted mean of the Esfordi syenite

of the Kiruna-type deposits (e.g., < 10 ppm Cr in the Chilean deposits; Nyström and Henriquez 1994 and 0.01–0.07 wt. % Cr_2O_3 in the Abagong deposit in China; Chai et al. 2014). The exception are samples from the Esfordi deposit which contain a higher Cr_2O_3 content (0.02–0.06 wt. %). The identification index of magnetite that was co-crystallizing with apatite in the Bafq-Saghand belt indicates that the high V content is also similar to that of Kiruna-type deposits (0.1 to 0.2 wt. %; Nyström and Henriquez 1994; Toplis and Corgne 2002) and Mn values range from 69.7 to 3175 ppm (Table 3; Fig. 13a, b), which is once more similar to that in Kiruna-type deposits (Nyström and Henriquez 1994). However, the Mn values (100–1000 ppm) are more similar to those from a high-temperature magmatic-hydrothermal fluid (c.f., Dare et al. 2012; Boutroy et al. 2014). Moreover, Mg is enriched up to six times in some samples relative to typical Kiruna-type deposits. The uncharacteristic Mg enrichment is, however, also seen in the iconic El Laco deposit in Chile, where a five times Mg enrichment and additional Ni-enrichment (250–100 ppm) have been observed (Nyström and Henriquez 1994; Tornos et al. 2017). Considering Ternary plots of Ca + Al + Mn, Ni/(Cr + Mn) and Ti + V presented by Beaudoin et al. (2011), magnetite samples from the Bafq-Saghand belt fall within the Kiruna-type, porphyry and skarn deposit regions of the diagram and only a small number of samples fall within the IOCG region of the plot (Fig. 13). Specifically, the samples from Esfordi deposit are commonly placed within the reference field of Kiruna-type deposits, while samples of the three other deposits (Chadormalu, Choghart and Se-Chahun) fall within the Skarn deposit range of the discrimination plots (Fig. 13a, b). A small number of magmatic samples from Esfordi, Se-Chahun and Choghart plot within the field of porphyry deposits (Fig. 13a, b). Generally, a linear trend from the Kiruna-type domain towards the porphyry and skarn deposit reference fields is observed in this figure (Fig. 13). This trend is comparable with, and highly correlated to, other iron oxide-apatite deposits and according to Huang et al. (2013, 2015), magmatic-hydrothermal magnetites are often concentrated in the range of skarn deposits on this diagram. The linear distribution of our magnetite samples along a skarn-porphyry-Kiruna-type lineage on a Ca + Al + Mn vs Ti + V diagram is, for instance, similar to in the Los Colorados Kiruna magmatic-hydrothermal iron deposits in Chilean Iron Belt (Kinpping et al. 2015a; b; Simon et al. 2018); (Fig. 13a). According to the diagram introduced by Dare et al. (2014) (Fig. 13h), which separates magmatic from hydrothermal magnetites, almost all of the analyzed samples fall within the domain of hydrothermal magnetites, but close to the field of magmatic magnetites. In other diagrams (Fig. 13c, g), which separate BIF-related magnetites, iron–titanium, and iron-apatite deposits from

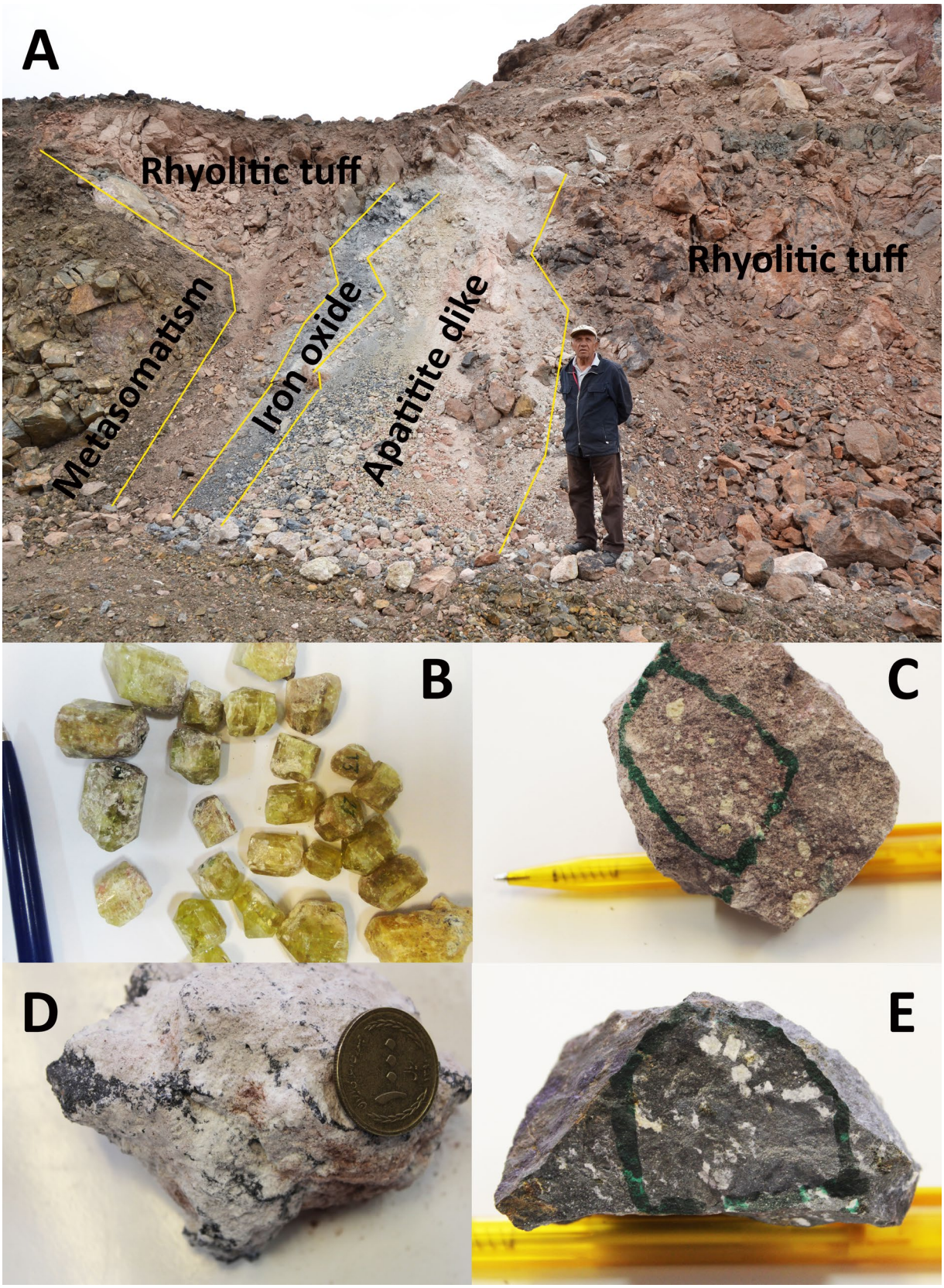

Fig. 10 Apatite mineralization in the Bafq-Saghand metallogenic belt. **a** fluorapatite crystals of the Esfordi deposit. **b** Large apatite crystals in metasomatised host rock. **c** Micro-crystalline of apatite in association with magnetite. **d** Magnetite with large crystals of syngenetic apatite of the Chador-Malu deposit. **e** Apatite and iron oxide intrusions in field relation with metasomatised country rock domains

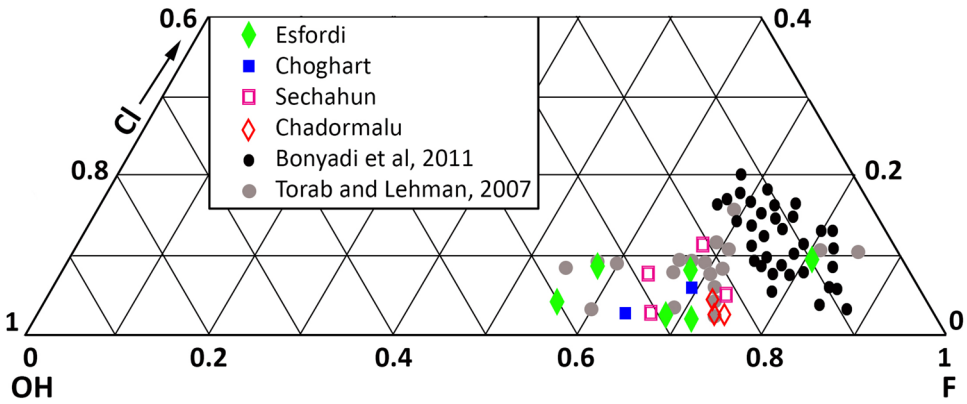

Fig. 11 F–OH–Cl Ternary diagram (after Piccoli and Candela 2002) of the apatite from the ores of the Bafq-Saghand metallogenic belt. The F–OH–Cl contents of the apatite samples are concentrated within the hydroxyl-fluorapatite domain of the diagram

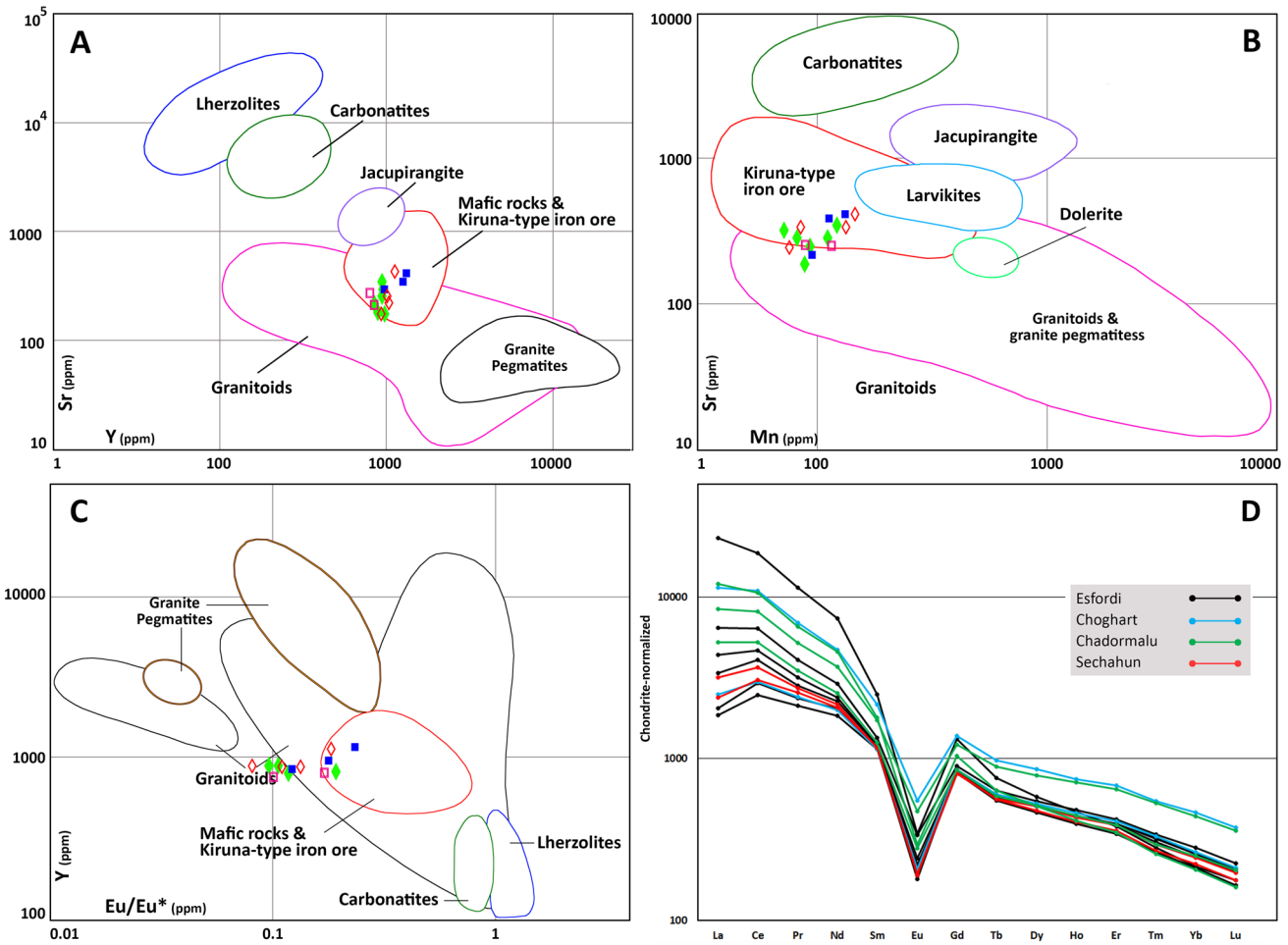

Fig. 12 **a** Sr–Y diagram. **b** Sr–Mn diagram. **c** Y–Eu/Eu* Diagram (Belousova et al. 2002). **d** Spider diagram of REEs—Normalized versus Chondrite (Chondrite data form Sun and McDonough 1989). Considering Sr vs Y contents (**a**), Sr vs Mn contents (**b**), and Y vs Eu/Eu* contents (**c**), the studied apatite crystals show values typical for mafic rocks and Kiruna-type deposits. **d** Patterns in a REE spider diagram normalized to chondrite indicate high depletion of Eu along with a strong contrast between LREEs and HREEs

each other (Lohberg and Horndhal 1983), it is obvious that almost all of the studied samples fall within the iron-apatite domain and are clearly separated from to the two other domains. The trace element data from magnetite thus support a magmatic to magmatic high-temperature hydrothermal origin for the Bafq-Saghand magnetites under study.

Oxygen isotopes

The $\delta^{18}O$ ratios of magnetite crystals were shown to be a useful tool to identify their mode of formation (Taylor 1967; Jonsson et al. 2013). A range of $\delta^{18}O$ of −0.4 to +4.9 ‰ is recorded. This range compares to crystallized magnetite from a felsic-intermediate magma at high temperatures (c.f., Taylor 1967; Jonsson et al. 2013; Troll et al. 2019). The $\delta^{18}O$ content of most of the magnetite samples varies between −0.1 and +2.2 ‰, and an enrichment beyond that in ^{18}O (+4.7 to +6.8 ‰) is recorded in four samples from brecciated tuff-altered magnetites (Table 5). Results revealed by analysis related to the enriched samples imply magnetite in isotopic equilibrium with rhyolite magma of ~ 10 ‰ (Fig. 14). It is notable that the $\delta^{18}O$ value of altered host rocks of Kiruna in Sweden ranges from +5 to +10 ‰, thus also slightly exceeding the common range of intermediate igneous rocks (+6 to +8 ‰) (Taylor, 1968; Jonsson et al. 2013) and consistent with recently reported rhyolite values of up to 10 ‰ in some active subduction zone settings (e.g., Budd et al. 2017). The $\delta^{18}O$ values of most of the studied magnetites (−0.1 to +2.2 ‰), however, fall clearly within the range of regular orthomagmatic to magmatic-hydrothermal magnetites similar to, e.g., the reported data from El Laco in Chile (Nyström et al. 2008), Kiruna and Grängesberg in Sweden (Nyström and Henriquez 1994; Jonsson et al. 2013), and the Zhibo and Chagangnoer deposits in China (Zhang et al. 2014) (Fig. 14). The $\delta^{18}O$ of the two samples of Esfordi deposit that range from +4.0 to +4.8 ‰ (Table 5; Fig. 14) then likely indicate magnetite crystallization from a crustally contaminated intermediate to felsic magma at a high temperature or subsequent alteration due to hydrothermal activity (e.g., Jonsson et al. 2013; Budd et al. 2017). The few $\delta^{18}O$ values below +0.3 ‰ ($n = 5$), in turn, indicate a degree of secondary oxidation and low-temperature hydrothermal alteration (e.g., Troll et al. 2019).

Ages of ore formation

Analysis of crystallization ages of monazites hosted in silica breccia units of the Choghart deposit yielded ages between 515 and 529 (± 21) Ma, as revealed by EPMA analysis (Torab and Lehman 2007). Stosch et al. (2011) studied apatites of the Choghart, Mishdowan, Lake-Siah, Zarigan and Gazestan areas using Thermal Ionization Mass Spectrometry (TIMS) and the U–Pb method, deriving ages of 527–539 Ma as the crystallization age of the apatites. Analysis of monazitic inclusions of apatites results in two different age groups of ~ 440 Ma (Choghart) and 133 to 140 ± 1 Ma (Gazestan). Notably, the age of the apatites hosting the young monazites is 523 Ma for the Choghart deposit which is younger than what was obtained from analyzing the apatites without any inclusions (Stosch et al. 2011). Hence, it was proposed that some amount of Pb has likely been lost during monazite mineralization. Younger dates (140 ± 1 and 133 ± 1 Ma) were related to the monazites of the Gazestan area and may link to an event of sericitic and potassic alteration. The date of the Esfordi and Chadormalu rhyolitic rocks, using ^{40}Ar–^{39}Ar on potassic feldspar samples from potassic alteration in rhyolitic rocks associated with the magnetite-apatite mineralization, was determined at 130.4 ± 1.2 and 158.6 ± 1.3 Ma (Torab 2008), which supports considerably later post-mineralization alteration processes that were possibly caused by tectonic activity during the Jurassic and Cretaceous eras (Verdel et al. 2007). It is notable that the apatites which have inclusions that produce ages that are a little younger than the different geological events are depleted in Pb content. Studies conducted by Bonyadi et al. (2011), for example, reveal the age of Se-Chahun apatites at 510 (± 8) Ma. Considering the lack of Pb during generation of Se-Chahun apatites, the determined age for the sample from this area may thus be slightly younger than the real geological age (Bonyadi et al. 2011).

Geodynamic origin of the Bafq-Saghand metallogenic belt

There are two leading hypothesis regarding the geodynamic setting of the Bafq-Saghand metallogenic belt: (1) continental rifting (Berberian and King 1981) and (2) subduction of a continental margin (Ramezani and Tucker 2003).

Geochemistry of igneous rocks and tectonic setting

Regarding the tectonic genesis of igneous rocks, a comprehensive study was carried out by Ramezani and Tucker (2003). Based on geochemical analysis, the rhyolitic rocks were proposed to be associated with the Cambrian leucogranites in the region. The Cambrian leucogranite's composition is calc-alkaline and considering geochemical studies of REEs and available age data, the geological age of these rocks overlaps with the Cambrian granitic complex (Ramezani and Tucker 2003). These rocks show depletion of Nb and Ta along with enrichment of Th in chondrite normalized spider diagrams and the genesis of the rhyolitic volcanic rocks, the Cambrian leucogranites, and the Cambrian granitoids of the Bafq-Saghand belt are thus subduction derived (Ramezani and Tucker 2003).

To cement and further refine these considerations, discrimination diagrams are plotted with our new data, especially Nb versus Y, Ta versus Yb, Rb versus Ta + Yb, and Rb versus Yb + Nb (e.g., Pearce et al. 1984). Two distinct series of magmatic rocks emerge. The first includes the

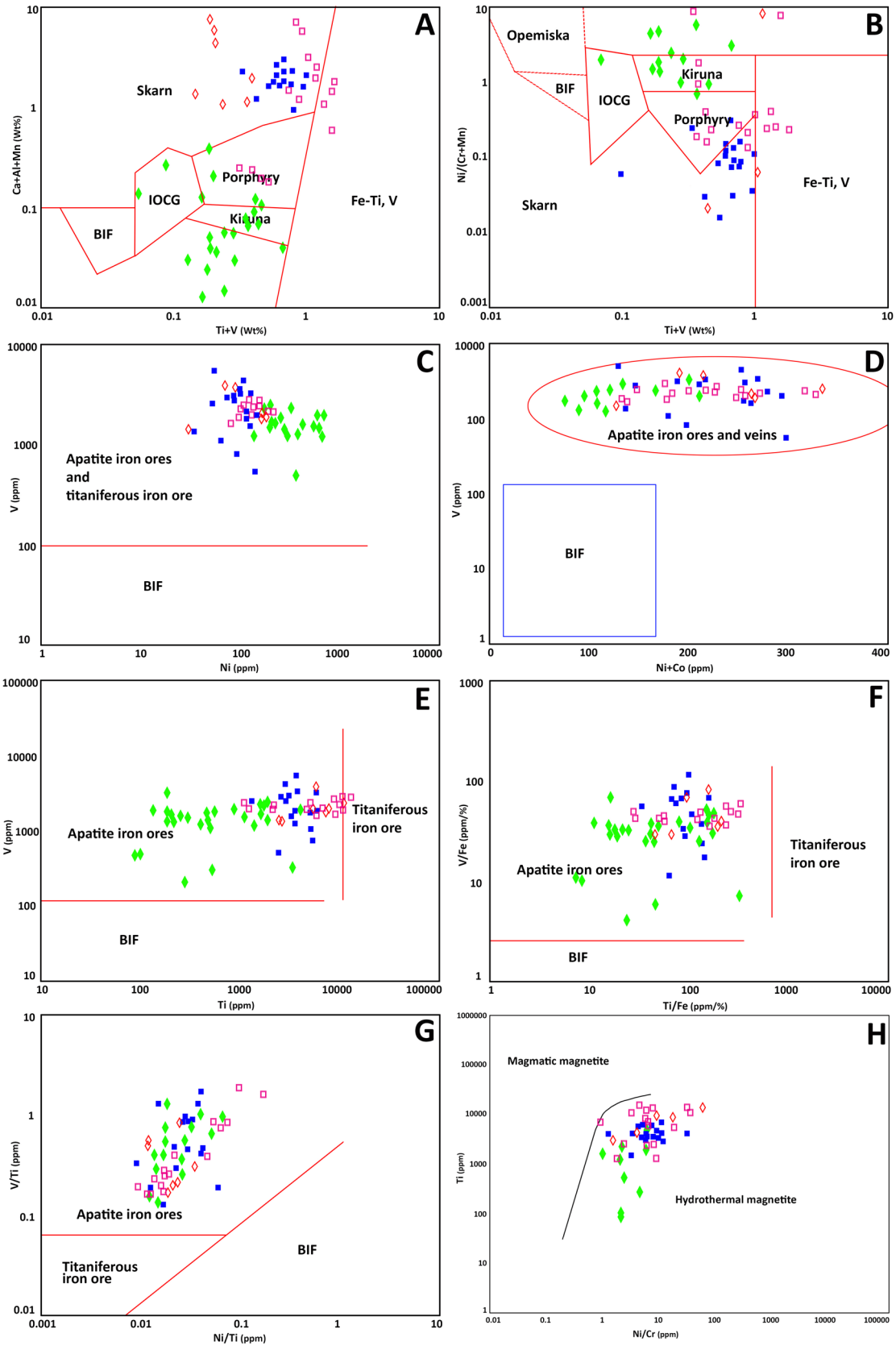
A
Skarn
Porphyry
IOCG
Fe-Ti, V
Kiruna
BIF
Ca+Al+Mn (Wt%)
Ti+V (Wt%)
B
Opemiska
BIF
IOCG
Kiruna
Porphyry
Fe-Ti, V
Skarn
Ni/(Cr+Mn)
Ti+V (Wt%)
C
Apatite iron ores
and
titaniferous iron ore
BIF
V (ppm)
Ni (ppm)
D
Apatite iron ores and veins
BIF
V (ppm)
Ni+Co (ppm)
E
Apatite iron ores
Titaniferous
iron ore
BIF
V (ppm)
Ti (ppm)
F
Apatite iron ores
Titaniferous
iron ore
BIF
V/Fe (ppm/%)
Ti/Fe (ppm/%)
G
Apatite iron ores
BIF
Titaniferous
iron ore
V/Ti (ppm)
Ni/Ti (ppm)
H
Magmatic magnetite
Hydrothermal magnetite
Ti (ppm)
Ni/Cr (ppm)

◂**Fig. 13** Geochemistry of magnetite of the Bafq-Saghand metallogenic belt. **a** and **b** The studied magnetite samples are plotted as Ca + Al + Mn and Ni/(Cr + Mn) vs Ti + V (after Dupuis and Beaudoin 2011). Our data follow a trend for skarn, porphyry and Kiruna-type deposits. **c–g** Based on Lohberg and Horndhal (1983) the magnetite samples plot in the apatite-rich iron ore domain and show no geochemical affinity with BIF or titaniferous iron ores. **h** The Magnetite samples plot in the hyrothermal domain on discrimination diagram (after Dare et al. 2014), but straddle the magmatic field

calc-alkaline intrusive bodies (Fig. 5), such as the Zarigan granites, Narigan and Chadormalu granites, which seemingly formed within a (calc-alkaline) magmatic arc environment (Fig. 15) and these bodies are introduced as part of the Cambrian granitoid complex, and the Cambrian leucogranite complex (Ramezani and Tucker 2003). The second group includes the alkaline magmatic bodies (Fig. 5) such as the Esfordi syenite and Narigan syenite which contrast the calc-alkaline suite and appear to reflect an intraplate tectonic setting (Fig. 15).

Integrating geodynamics with radiogenic dating of igneous rocks

The oldest rocks of the Bafq-Saghand region formed as part of the Tashk complex, which was deposited through the Late Neoproterozoic to Early Cambrian (627–533 Ma) (Ramezani and Tucker 2003). The metamorphosed Boneh-Shurow complex consists of five parts, namely (1) gray–pinkish mylonitic orthogneiss or protogneiss as protolith to the Boneh-Shurow gneiss (544 ± 7 Ma), (2) a mica-schist unit (617–602 Ma), (3) a garnet-amphibolite unit which likely reflects peak-metamorphism for the Boneh-Shurow (547.6 ± 2 Ma), (4) a quartz-dioritic unit (547.6 ± 2.5 Ma) and (5) mylonitic schists (Ramezani and Tucker 2003). The Sar-Kuh complex is located in the Sar-Kuh mountains in the North-Eastern part of Zarigan. This complex is divided into two main parts: (a) one with garnet-schist, staurolite, andalusite, mica-schist, amphibolite and metamorphosed volcano-sedimentary units. This part is intruded by several acidic porphyritic bodies. (b) The second part is composed of calcic-Dolomitic Marbles (Haghipour 1977), which are proposed to be Pre-Cambrian or Late Pre-Cambrian in age (Ramezani and Tucker 2003). The Cambrian Volcano-Sedimentary Unit (Ramezani 1997) covers the Upper-Proterozoic rocks (particularly the Tashk unit) and has an Early Cambrian age (528 Ma) and is associated with basement rhyodacites of the Duzakh-Dareh area. This unit includes the iron oxide-apatite deposits of the Bafq-Saghand metallogenic belt, which were previously considered as Cambrian or Eocambrian (Huckriede et al. 1962; Stöcklin 1968; Haghipour and Pelissier 1977). The age of the basal rhyodacite (528.2 ± 0.8 Ma) indicates an Early Cambrian age for the Cambrian Volcano-Sedimentary Unit and its equivalents (Rizu and Dezu series) in central Iran. An Early Cambrian age is recorded for the Rizu and Dezu series which are located in Zebar-Kuh at northeast of the Bafq-Saghand area (Sahandi et al. 1984). Early Cambrian carbonates within this formation unconformably cover the red sandstones and conglomerates of the lower Cambrian Lalun/Dahu formation within the Zarigan and Bafq area (Förster and Jafarzadeh 1994). U–Pb dating analysis of zircon related to the Chapedony complex indicates an Eocene geological age (Ramezani and Tucker 2003). Other studies proposed that this complex developed during the Tertiary and is a metamorphosed igneous complex related to Eocene magmatic activity (Verdel et al. 2007; Kargaranbafghi et al. 2008; Yassaghi and Masoodi 2011; Kargaranbafghi et al. 2012, 2015).

The Cambrian Ariz granitoids (533 ± 1 Ma), the Cambrian Zarigan, Narigan and Chadormalu leucogranites (525 to 526 ± 1 Ma), and the Eocene post-metamorphic bodies are three magmatic complexes intruded into the Bafq-Saghand belt (Ramezani and Tucker 2003). It is notable that alkaline bodies such as the Esfordi syenite (Arash syenite; Valizadeh and Sharifi 2004) and the Narigan syenite (Afshin syenite) have intruded into the Cambrian Volcano-Sedimentary Unit and cover a vast area. These alkaline bodies were previously reported as gabbro units with the same geological age as the Cambrian granitoids, but without any radiometric dating available (Valizadeh and Sharifi 2004). Therefore, samples from these units were collected and analyzed using the U–Pb dating method (Table 6). Specifically, we separated zircon grains ($n = 22$) from the Esfordi syenite in the Northern part of the Esfordi deposit (Fig. 9a) and from the Narigan syenite in the Eastern part of Narigan village (Fig. 9b) and analyzed 10 to 12 points on each crystal (Table 6). From the resulting U–Pb data, average crystallization ages for zircon were determined and resulted in a radiometric age of 430 ± 9 Ma, but a concordia diagram of $^{206}Pb/^{238}U$ vs $^{207}Pb/^{235}U$ yields an age of 441 ± 6 Ma, and the two ages overlap within the given uncertainties (Fig. 9).

Considering the previous research cited above on the geochemistry of magmatic, metamorphic and clastic rocks and taking into account the whole rock geochemical data and U–Pb dating analysis of this study, there are three orogenic events recorded within the Bafq-Saghand region. These occurred in the Late Neoproterozoic to Early Cambrian, the Late Triassic, and in the Eocene. In terms of chronology, degree of metamorphism, calc-alkaline plutonism, rhyolitic-andesitic volcanism and geological setting of trondhjemite, the oldest orogenic event of this area occurred around 547–525 Ma. This Late Neoproterozoic–Early Cambrian orogenic event of the Central Iran zone is related to a magmatic arc which extended along the coast of the Gondwana supercontinent with the Proto-Tethys Ocean (cf. Ramezani and Tucker 2003). Recent research on the early Cimmerian orogenic event in the Saghand area discovered late Triassic

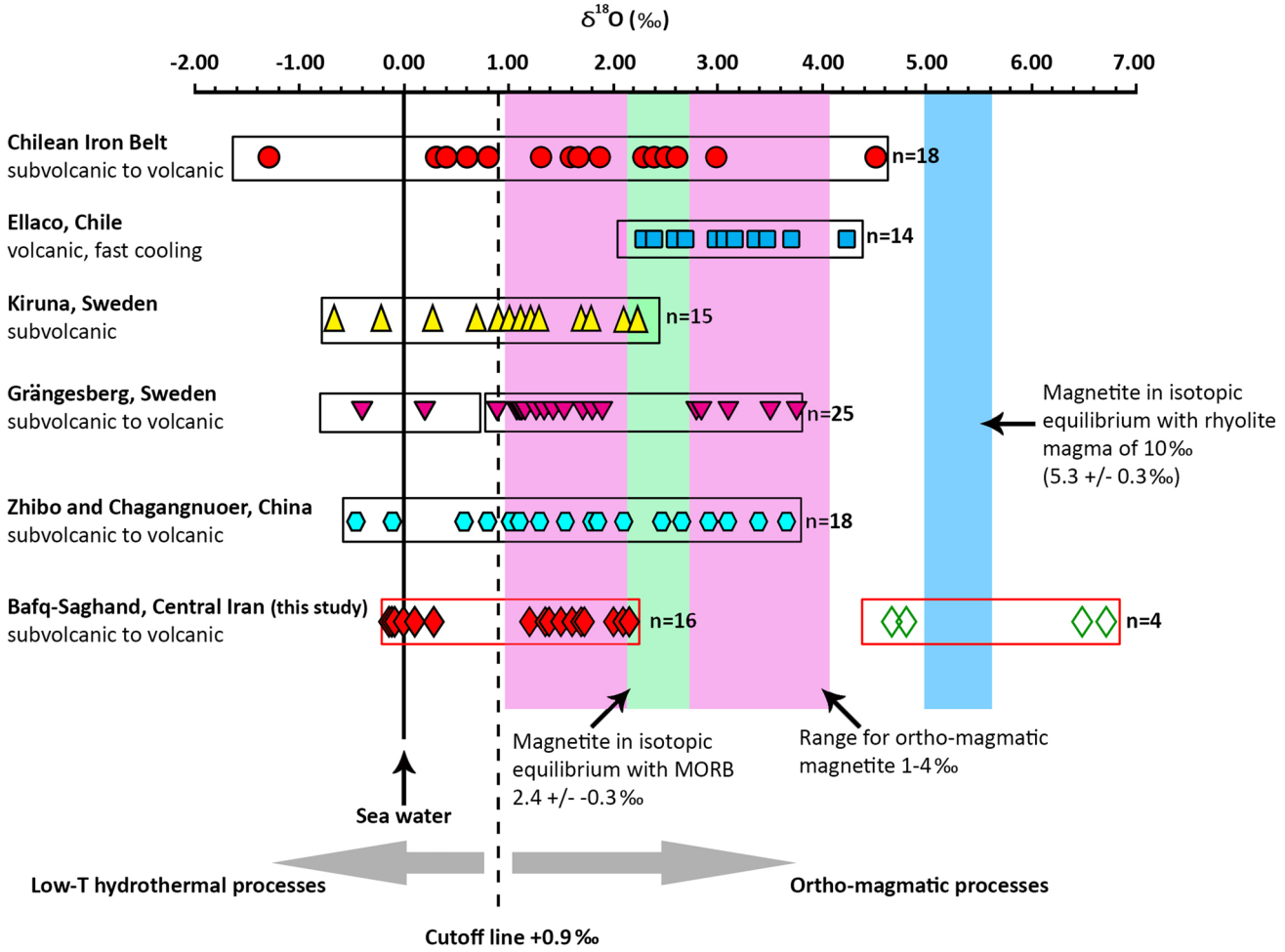

Fig. 14 Magnetite samples $\delta^{18}O$ values from Bafq-Saghand metallogenic belt (this study) compared to other iron ore deposits (modified after Troll et al. 2019). The present magnetite samples plot dominantly above the + 0.9 ‰ in the field of high-temperature ortho-magmatic magnetites (~ 800–1000 ℃). The samples that plot below + 0.9 ‰ reflect mineralization derived from lower temperature (hydrothermal) processes

magmatic bodies, and hence a tectono-magmatic event which formed within a collisional environment. The Late Triassic orogenic event (220–213 Ma) is identified based on intrusions of granitic-tonalitic magmatic bodies (Ramezani and Tucker 2003). Finally, the distribution of metamorphic rocks, migmatites and post-kinematic magmatic rocks of 47–44 Ma within the western part of the Saghand area is indicative of an influence of the Early Alpine Orogeny due to convergence between the Arabian and Eurasian plates (Ramezani and Tucker 2003). Currently, residual clasts of this border, including the Central Iran zone, are covered by deposits from the Alpine-Himalayan orogenic belt and closure of the Tethys Ocean occurred after completion of the Alpine–Himalayan subduction process. Geochemistry and the calc-alkaline nature as well as the tectonic setting of the Zarigan, Narigan, Chadormalu and Ariz magmatic bodies confirms the idea of orogenic activities and generation of successive magmatic arcs within the Bafq-Saghand belt, which itself is located in the central part of the Kashmar–Kerman tectonic zone. However, based on age dating published by Ramezani and Tucker (2003) initial (Late Neoproterozoic–Early Cambrian—547–525 Ma) subduction and formation of a magmatic have occurred along the Gondwana border and resulted from subduction of parts of the Proto-Tethys Ocean (Fig. 16).

In contrast, the alkaline magmatic bodies of the Bafq-Saghand belt such as Esfordi and Narigan show signatures of generation within a continental rift environment (continental granites). In comparison with calc-alkaline bodies, the mentioned alkaline magmatic bodies show a distinctive phase but were previously misinterpreted. Valizadeh and Sharifi (2004) considered these bodies as subduction related, but Balaghi et al. (2011) proposed a continental rifting event in the Late Neoproterozoic–Early Cambrian.

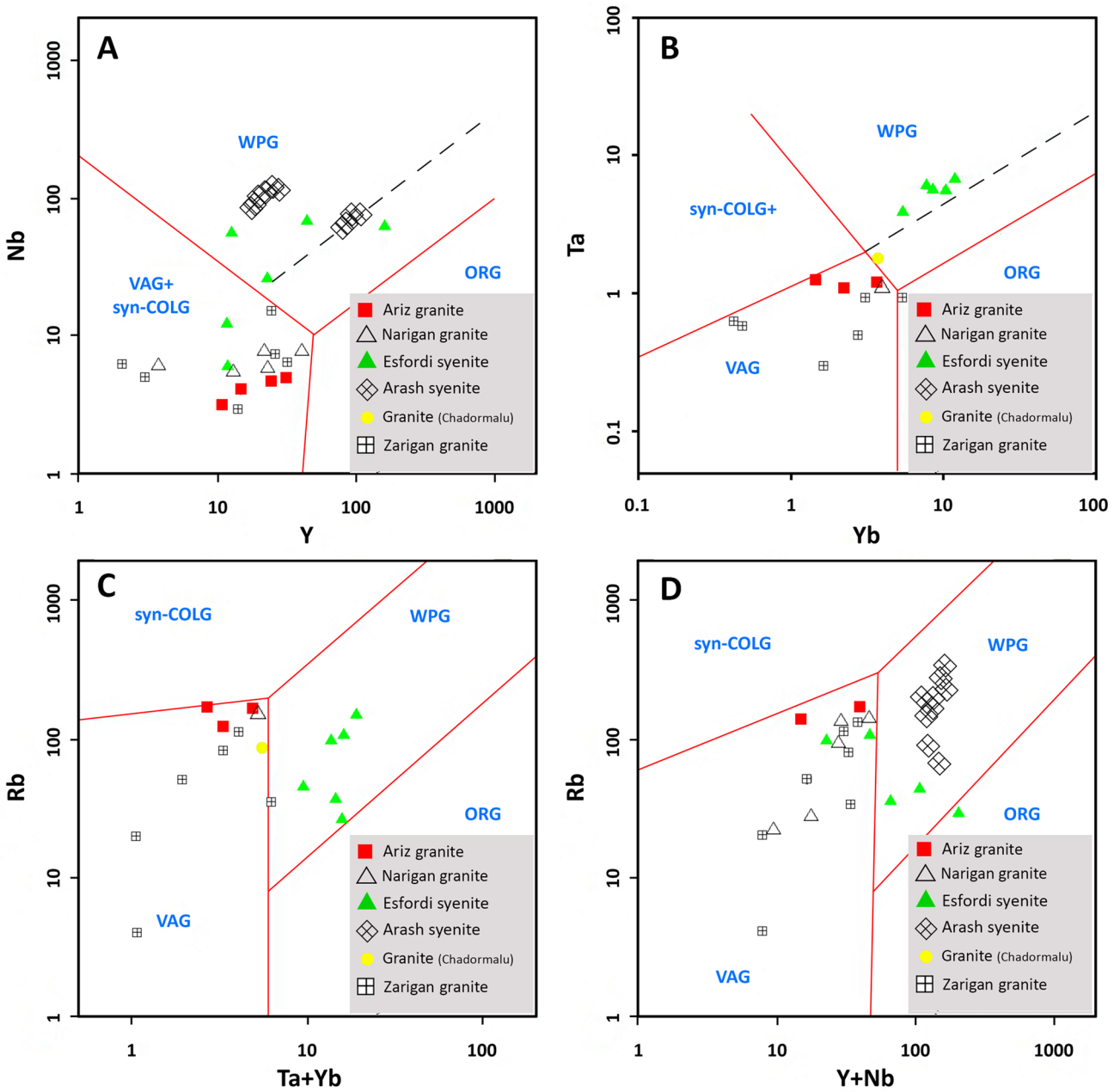

Fig. 15 Tectonic setting discrimination diagrams (after Pearce et al. 1984) on the basis of Nb versus Y, Ta versus Yb, Rb versus Ta + Yb, and Rb versus Yb + Nb. Two distinct series of magmatic rocks emerge. The first includes the calc-alkaline intrusive bodies, which seemingly formed within a magmatic arc environment. The second group includes the alkaline magmatic bodies, which contrast the calc-alkaline suite and appear to reflect an intraplate tectonic setting

Our new crystallization ages of the alkaline bodies (430 ± 9 and 441 ± 6 Ma) (Table 6; Fig. 9) now allow us to confirm that the Late Neoproterozoic–Early Cambrian magmatic arc at 525 to 547 Ma, which formed as a result of processes related to subduction of Proto-Tethys under continental border of Gondwana, was followed by continental rifting event between the Ordovician and Silurian within the Bafq-Saghand area at approximately 430–440 M.

Conclusion

We propose that the main iron mineralization event in this region relates to the older continental arc-type geodynamic event in the region (Fig. 16a) that is represented by calc-alkaline subduction-related tonalite, trondhjemite, granodioritic, dioritic and granitic magmatic bodies emplaced at ca. 525—532 Ma and the arc-related volcanic host

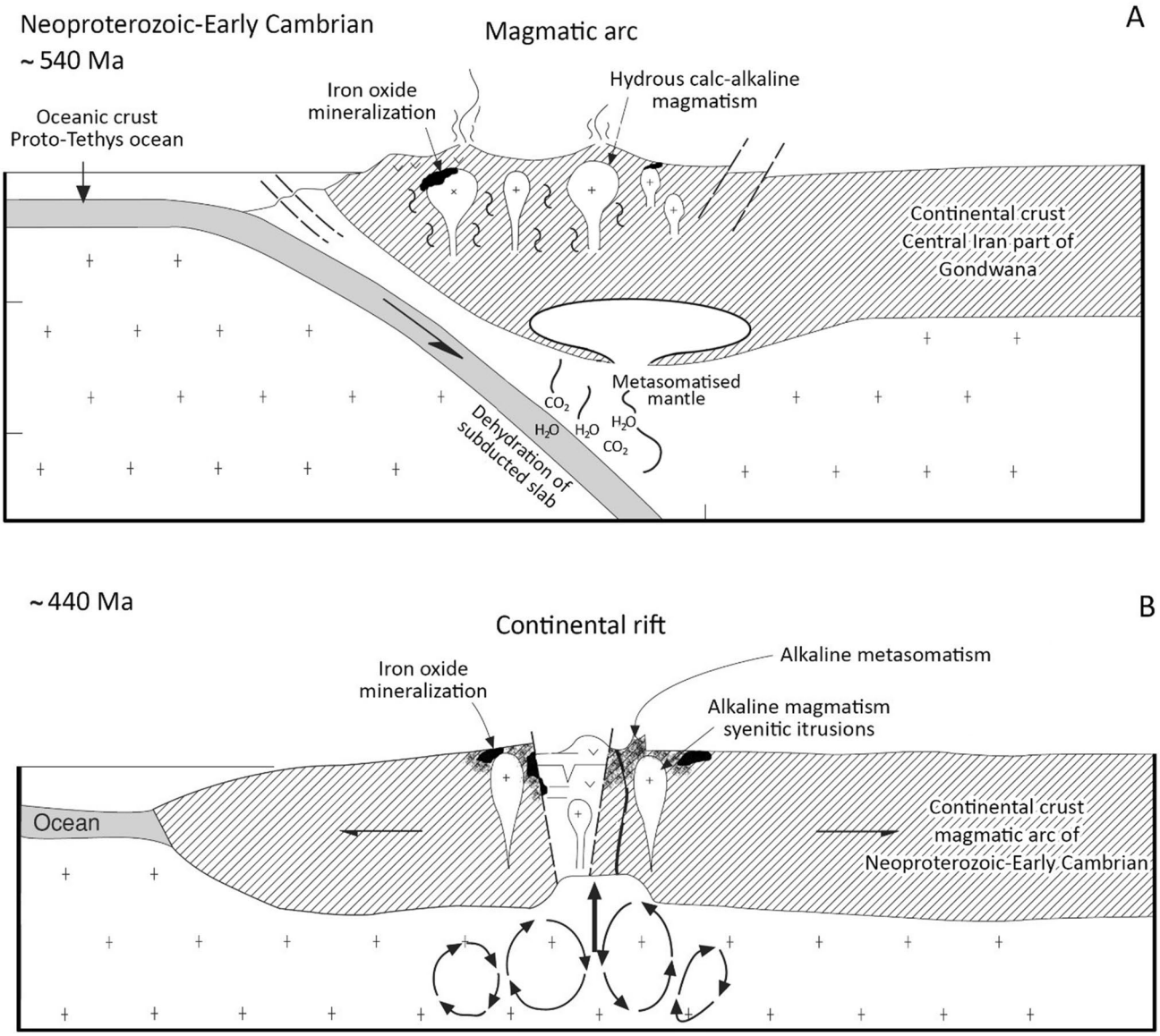

Fig. 16 Schematic representation of geodynamic episodes recorded in the Bafq-Saghand area. **a** Subduction of Proto-Tethys ocean under the Gondwana supercontinent. Central Iran is a part of the supercontinent and original mineralization of iron oxide that resulted from calc-alkaline magmatism at this time (~540 Ma). **b** subsequent rifting within the Bafq-Saghand area (~440 Ma) resulted in alkaline magmatism and caused (alkaline) metasomatism that effected the primary mineralization in the region and caused local mobilization and reprecipitation of iron ore that originally formed at ca 540 Ma

rock in the region. These granitoids and arc-type volcanic rocks show the same geological age as the iron oxide ores (ca. 510–539 Ma). According to trace element data of magnetite, apatite and $\delta^{18}O$ isotope data of magnetite, we also conclude that magmatic arc-type processes have played the main role in generation of iron oxide-apatite mineral deposits. However, during a later geodynamic episode, intrusion of alkaline syenite and monzosyenite bodies (421–447 Ma) occurred within a continental rift setting and primary magmatic mineralization was locally leached and redeposited through secondary hydrothermal processes (Fig. 16b). The younger monazites of Choghart (440 Ma) may have resulted from this hydrothermal event. The youngest geodynamic event in the region, the Alpine–Himalayan collision is calc-alkaline in nature but does not overlap in terms of radiometric ages. We thus conclude that the formation of low Ti iron-apatite ore within the Bafq-Saghand metallogenic belt was the result of high-temperature magmatic and hydrothermal processes associated with subduction-related calc-alkaline magmatism during the subduction of Proto-Tethys Ocean under the Gondwana supercontinent at 539–510 Ma, but was

hydrothermally affected by later rifting related alkaline magmatism at ~ 440 Ma.

Acknowledgements This is a contribution to Geological Survey of Iran for the XRF, ICP-OES and ICP-MS analysis at Central laboratory in Tehran and we would like to thak Mohamad Taghi Korei and Mohammadreza Hezareh for the analysis coordination in the Geological Survey of Iran, Tehran, Iran. The authors also acknowledge Chris Harris for O isotope analysis in Department of Geological Science in University of Cape Town. They also thank Mohammad Lotfi and Mohammad Hashem Emami for help during fieldwork and discussion of their study.

References

Aftabi A, Mohseni S, Babeki A, Azaraien H (2009) Fluid inclusion and stable isotope of the Esfordi Apatite-Magnetite deposit, Central Iran—a discussion. Econ Geol 104:137–139

Anderson T (2002) Correction of common lead in U–Pb analyses that do not report ^{204}Pb. Chem Geol 192:59–79

Angerer T, Hagemann SG, Danyushevsky LV (2012) Geochemical evolution of the banded iron formation-hosted high-grade iron ore system in the Koolyanobbing Greenstone Belt, Western Australia. Econ Geol 107:599–644

Arndt NT, Naldrett AJ, Pyke DR (1977) Komatiitic and iron-rich tholeiitic lavas of Munro Township, northeast Ontario. J Petrol 18:319–369

Ayers JC, Watson EB (1993) Apatite/fluid partitioning of rare-earth elements and strontium: experimental results at 1.0 GPa and 1000 C and application to models of fluid-rock interaction. Chem Geol 110:299–314

Balaghi Z, Sadeghian M, Ghasemi H (2011) Petrogenesis of the lower Paleozoic igneous rocks, south of Bahabad (bafq, Central Iran): implication for rifting. Petrology 1:45–64

Barton MD, Johnson DA (1996) Evaporitic-source model for igneous-related Fe oxide–(REE–Cu–Au–U) mineralization. Geology 24:259–262

Belousova EA (2000) Trace elements in zircon and apatite: application to petrogenesis and mineral exploration. Macquarie University, Australia, p 430

Belousova EA, Walters S, Griffin WL, O'Reilly SY (2001) Trace-element signatures of apatites in granitoids from the Mt Isa Inlier, northwestern Queensland. Aust J Earth Sci 48:603–619

Belousova EA, Griffin WL, O'Reilly SY, Fisher NI (2002) Apatite as an indicator mineral for mineral exploration: trace-element compositions and their relationship to host rock type. J Geochem Explor 76:45–69

Berberian M, King GCP (1981) Towards a paleogeography and tectonic evolution of Iran. Can J Earth Sci 18:210–265

Bonyadi Z, Davidson GJ, Mehrabi B, Meffre S, Ghazban F (2011) Significance of apatite REE depletion and monazite inclusions in the brecciated Se–Chahun iron oxide–apatite deposit, Bafq district, Iran: insights from paragenesis and geochemistry. Chem Geol 281:253–269

Boomeri M (2012) Rare earth minerals in Esfordi magnetite-apatite ore deposit, Bafq district. Ulum-I Zamin J Iran 22:71–82

Boutroy E, Dare SA, Beaudoin G, Barnes SJ, Lightfoot PC (2014) Magnetite composition in Ni–Cu–PGE deposits worldwide: application to mineral exploration. J Geochem Explor 145:64–81

Broughm SG, Hanchar JM, Tornos F, Westhues A, Attersley S (2017) Mineral chemistry of magnetite from magnetite-apatite mineralization and their host rocks: examples from Kiruna, Sweden, and El Laco, Chile. Miner Depos 52:1223–1244

Budd AD, Troll VR, Deegan FM, Jolis EM, Smith VC, Whitehouse MJ, Harris C, Freda C, Hilton DR, Halldórsson SA, Bindeman IN (2017) Magma reservoir dynamics at Toba caldera, Indonesia, recorded by oxygen isotope zoning in quartz. Sci Rep 7:40624

Chai F, Yang F, Liu F, Santosh M, Geng X, Li Q, Liu G (2014) The Abagong apatite-rich magnetite deposit in the Chinese Altay Orogenic Belt: a Kiruna-type iron deposit. Ore Geol Rev 57:482–497

Chen WT, Zhou MF, Gao JF, Hu R (2015) Geochemistry of magnetite from Proterozoic Fe–Cu deposits in the Kangdian metallogenic province, SW China. Miner Depos 50:795–809

Chiu HY, Chung SL, Wu FY, Liu D, Liang YH, Lin IJ, Iizuka Y, Xie LW, Chu MF (2009) Zircon U–Pb and Hf isotopic constraints from eastern Transhimalayan batholiths on the precollisional magmatic and tectonic evolution in southern Tibet. Tectonophysics 477:3–19

Clark AH, Kontak DJ (2004) Fe–Ti–P oxide melts generated through magma mixing in the Antauta Subvolcanic Center, Peru: implications for the origin of nelsonite and iron oxide-dominated hydrothermal deposits. Econ Geol 99:377–395

Daliran F (1990) The magnetite apatite deposit of Mishdovan. Eastcentral Iran, an alkaline rhyolite hosted "Kiruna Type" occurrence in the Bafq metallotect (Mineralogic, Petrographic and geochemical study of the ores and the host rocks): Heidelberger Geowiss Abh, 37.

Daliran F (2002) Kiruna-type iron oxide-apatite ores and apatitites of the Bafq district Iran with an emphasis on the REE geochemistry of their apatites. In: Porter TM (ed) Hydrothermal iron oxide copper gold & related deposits: a global perspective, vol 2. PGC Publishing, Adelaide, pp 303–320

Dare SA, Barnes SJ, Beaudoin G (2012) Variation in trace element content of magnetite crystallized from a fractionating sulfide liquid, Sudbury, Canada: implications for provenance discrimination. Geochim Cosmochim Acta 88:27–50

Dare SA, Barnes SJ, Beaudoin G, Méric J, Boutroy E, Potvin-Doucet C (2014) Trace elements in magnetite as petrogenetic indicators. Miner Depos 49:785–796

Darvishzadeh A (1983) Investigation on Esfordi phosphate deposit. J Sci Univ Tehran. 2–24

Deymar S, Yazdi M, Rezvanianzadeh MR, Behzadi M (2018) Alkali metasomatism as a process for Ti–REE–Y–U–Th mineralization in the Saghand Anomaly 5, Central Iran: insights from geochemical, mineralogical, and stable isotope data. Ore Geol Rev 93:308–336

Dmitrijeva M, Metcalfe AV, Ciobanu CL, Cook NJ, Frenzel M, Keyser WM, Ehrig K (2018) Discrimination and variance structure of trace element signatures in Fe-oxides: a case study of BIF-mineralisation from the Middleback ranges, South Australia. Math Geosci 50:381–415

Dupuis C, Beaudoin G (2011) Discriminant diagrams for iron oxide trace element fingerprinting of mineral deposit types. Miner Depos 46:319–335

Förster H, Borumandi H (1971) Jungpräkambrische Magnetit-Lava und Magnetit-Tuffe aus dem Zentraliran. Naturwissenschaften 58:524–524

Förster H, Jafarzadeh A (1994) The Bafq mining district in central Iran; a highly mineralized Infracambrian volcanic field. Econ Geol 89:1697–1721

Frietsch R (1978) On the magmatic origin of iron ores of the Kiruna type. Econ Geol 73:478–485

Frietsch R, Perdahl JA (1995) Rare earth elements in apatite and magnetite in Kiruna-type iron ores and some other iron ore types. Ore Geol Rev 9:489–510

Frost BR, Frost CD (2008) A geochemical classification for feldspathic igneous rocks. J Petrol 49:1955–1969

Ghazi JM, Harris C, Rahgoshay M, Moazzen M (2019) Combined igneous and hydrothermal source for the Kiruna-type Bafq magnetite-apatite deposit in Central Iran; trace element and oxygen isotope studies of magnetite. Ore Geol Rev 105:590–604

Grigsby JD (1990) Detrital magnetite as a provenance indicator. J Sediment Res 60:940–951

Groves DI, Bierlein FP, Meinert LD, Hitzman MW (2010) Iron oxide copper-gold (IOCG) deposits through earth history: implications for origin, lithospheric setting, and distinction from other epigenetic iron oxide deposits. Econ Geol 105:641–654

Haghipour A, Pelissier G (1977) Geological map of the Biabanak-Bafq area. Geological Survey of Iran, Tehran

Haghipour A, Bolourchi M, Houshmandzadeh A, Sabzehei M, Stöcklin J, Hubber H, Sluiter W, Aghanabati A (1977) Exploration text of the Ardekan Quderanglemap. Geological Survey of Iran, Tehran, pp 1–88

Harlov DE, Andersson UB, Förster HJ, Nyström JO, Dulski P, Broman C (2002) Apatite–monazite relations in the Kiirunavaara magnetite–apatite ore, northern Sweden. Chem Geol 191:47–72

Harris C, Ashwal LD (2002) The origin of low $\delta\ ^{18}O$ granites and related rocks from the Seychelles. Contrib Miner Petrol 143:366–376

Harris C, Vogeli J (2010) Oxygen isotope composition of garnet in the Peninsula Granite, Cape Granite Suite, South Africa: constraints on melting and emplacement mechanisms. S Afr J Geol 113:401–412

Heidarian H, Alirezaei S, Lentz DR (2017) Chadormalu Kiruna-type magnetite-apatite deposit, Bafq district, Iran: Insights into hydrothermal alteration and petrogenesis from geochemical, fluid inclusion, and sulfur isotope data. Ore Geol Rev 83:43–62

Heidarian H, Lentz DR, Alirezaei S, McFarlane CR, Peighambari S (2018) Multiple stage ore formation in the chadormalu iron deposit, Bafq Metallogenic Province, Central Iran: evidence from BSE imaging and apatite EPMA and LA-ICP-MS U–Pb Geochronology. Minerals 8:87

Henríquez F, Martin RF (1978) Crystal-growth textures in magnetite flows and feeder dykes, El Laco, Chile. Can Mineral 16:581–589

Hitzman MW (2000) Iron Oxide–Cu–Au deposits: what, where, when, and why. In: Porter TM (ed) Hydrothermal iron oxide copper-gold and related deposits: a global perspective, vol 1. PGC Publishing, Adelaide, pp 9–25

Hitzman MW, Oreskes N, Einaudi MT (1992) Geological characteristics and tectonic setting of Proterozoic iron oxide (Cu–U–Au–REE) deposits. Precambr Res 58:241–287

Hou T, Zhang Z, Kusky T (2011) Gushan magnetite–apatite deposit in the Ningwu basin, lower Yangtze river valley, SE China: hydrothermal or Kiruna-type? Ore Geol Rev 43:333–346

Hu H, Li JW, Harlov DE, Lentz DR, McFarlane CR, Yang YH (2020) A genetic link between iron oxide-apatite and iron skarn mineralization in the Jinniu volcanic basin, Daye district, eastern China evidence from magnetite geochemistry and multi-mineral U–Pb geochronology. Bulletin 132:899–917

Huang XW, Zhou MF, Qi L, Gao JF, Wang YW (2013) Re–Os isotopic ages of pyrite and chemical composition of magnetite from the Cihai magmatic–hydrothermal Fe deposit, NW China. Mineralium Deposita 48:925–946

Huang XW, Gao JF, Qi L, Zhou MF (2015) In-situ LA-ICP-MS trace elemental analyses of magnetite and Re–Os dating of pyrite: the Tianhu hydrothermally remobilized sedimentary Fe deposit, NW China. Ore Geol Rev 65:900–916

Huckriede R, Kürsten M, Venzlaff H (1962) Zur geologie des gebiets zwischen Kerman und Saghand (Iran). Beihefte zum Geologischen Jahrbuch 51:1–197

Irvine TNJ, Baragar WRAF (1971) A guide to the chemical classification of the common volcanic rocks. Can J Earth Sci 8:523–548

Jackson SE, Pearson NJ, Griffin WL, Belousova EA (2004) The application of laser ablation-inductively coupled plasma-mass spectrometry to in situ U–Pb zircon geochronology. Chem Geol 211:47–69

Jami M (2005) Geology, geochemistry and evolution of the Esfordi phosphate-iron deposit, Bafq area, Central Iran. Doctoral dissertation, University of New South Wales

Jami M, Dunlop AC, Cohen DR (2007) Fluid inclusion and stable isotope study of the Esfordi apatite-magnetite deposit, Central Iran. Econ Geol 102:1111–1128

Jenner GA, Longerich HP, Jackson SE, Fryer BJ (1990) ICP-MS–a powerful tool for high-precision trace-element analysis in earth sciences: evidence from analysis of selected USGS reference samples. Chem Geol 83:133–148

Jonsson E, Troll VR, Högdahl K, Harris C, Weis F, Nilsson KP, Skelton A (2013) Magmatic origin of giant 'Kiruna-type'apatite-iron-oxide ores in Central Sweden. Sci Rep 3:1–8

Kargaranbafghi F, Foeken JP, Neubauer F, Stuart FM (2008) How Chapedony metamorphic core complex (Central Iran) became cool and how it was overprinted by Neogene asthenosphere uprise: inferences from (U–Th)/He thermochronology. Geophysical Research Abstracts 10

Kargaranbafghi F, Neubauer F, Genser J, Faghih A, Kusky T (2012) Mesozoic to Eocene ductile deformation of western Central Iran: from Cimmerian collisional orogeny to Eocene exhumation. Tectonophysics 564:83–100

Kargaranbafghi F, Neubauer F, Genser J (2015) Rapid Eocene extension in the Chapedony metamorphic core complex, Central Iran: constraints from 40 Ar/39 Ar dating. J Asian Earth Sci 106:156–168

Kimura JI, Yamada Y (1996) Evaluation of major and trace element analysis using a flux to some ratio of two to one glass beads. J Mineral Petrol Econ Dev 91:62–72

Knipping JL, Bilenker LD, Simon AC, Reich M, Barra F, Deditius AP, Munizaga R (2015a) Giant Kiruna-type deposits form by efficient flotation of magmatic magnetite suspensions. Geology 43:591–594

Knipping JL, Bilenker LD, Simon AC, Reich M, Barra F, Deditius AP, Munizaga R (2015b) Trace elements in magnetite from massive iron oxide-apatite deposits indicate a combined formation by igneous and magmatic-hydrothermal processes. Geochim Cosmochim Acta 171:15–38

Kolker A (1982) Mineralogy and geochemistry of Fe-Ti oxide and apatite (nelsonite) deposits and evaluation of the liquid immiscibility hypothesis. Econ Geol 77:1146–1158

Le Bas MJ, Lemaitre RW, Streckeisen A, Zanettin B (1986) A chemical classification of volcanic-rocks based on the total alkali silica diagram. J Petrol 27:745–750

Loberg BE, Horndahl AK (1983) Ferride geochemistry of Swedish Precambrian iron ores. Miner Depos 18:487–504

Ludwig KR (2003) User's manual for IsoPlot 3.0. A geochronological toolkit for Microsoft Excel 71

Majidi SA (2015) Metallogeny of iron oxide, apatite and rare earth elements in the Bafq-Saghand Area, Central Iran. PhD thesis. Tehran, Iran, pp 1–105

Meyer C (1988) Ore deposits as guides to geologic history of the Earth. Annu Rev Earth Planet Sci 16:147–171

Mohseni S, Aftabi A (2012) Comment on "Significance of apatite REE depletion and monazite inclusions in the brecciated Sehchahun iron oxide–apatite deposit, Bafq district, Iran: Insights from paragenesis and geochemistry" by Bonyadi, Z., Davidson, GJ, Mehrabi, B., Meffre, S., Ghazban, F [Chem. Geol. 281, 253–269]. Chem Geol 334:378–381

Mohseni S, Aftabi A (2015) Structural, textural, geochemical and isotopic signatures of synglaciogenic Neoproterozoic banded iron formations (BIFs) at Bafq mining district (BMD), Central Iran: the possible Ediacaran missing link of BIFs in Tethyan metallogeny. Ore Geol Rev 71:215–236

Mokhtari MAA, Zadeh GH, Emami MH (2013) Genesis of iron-apatite ores in Posht-e-Badam Block (Central Iran) using REE geochemistry. J Earth Syst Sci 122:795–807

Moore F, Modabberi S (2003) Origin of Choghart iron oxide deposit, Bafq mining district, Central Iran: new isotopic and geochemical evidence. J Sci Islam Rep Iran 14:259–270

Mücke A, Younessi R (1994) Magnetite-apatite deposits (Kiruna-type) along the Sanandaj-Sirjan zone and in the Bafq area, Iran, associated with ultramafic and calcalkaline rocks and carbonatites. Mineral Petrol 50:219–244

Nadoll P, Mauk JL, Hayes TS, Koenig AE, Box SE (2012) Geochemistry of magnetite from hydrothermal ore deposits and host rocks of the Mesoproterozoic Belt Supergroup, United States. Econ Geol 107:1275–1292

Nadoll P, Angerer T, Mauk JL, French D, Walshe J (2014) The chemistry of hydrothermal magnetite: a review. Ore Geol Rev 61:1–32

Naslund HR, Henríquez F, Nyström JO, Vivallo W, Dobbs FM (2002) Magmatic iron ores and associated mineralisation: examples from the Chilean High Andes and Coastal Cordillerain. In: Porter TM (ed) Hydrothermal iron oxide copper-gold and related deposits: a global perspective, pp 207–226

Nikolenko AM, Redina AA, Doroshkevich AG, Prokopyev IR, Ragozin AL, Vladykin NV (2018) The origin of magnetite-apatite rocks of Mushgai-Khudag Complex, South Mongolia: mineral chemistry and studies of melt and fluid inclusions. Lithos 320:567–582

Niktabar SM, Omran NR (2018) Geochemistry and petrology of rift-related mafic sills and arc-related Gabbro-Diorite bodies, Northern Bafq District, Central Iran. Acta Geochim 37:180–192

Nyström JO, Henríquez F (1994) Magmatic features of iron ores of the Kiruna type in Chile and Sweden: ore textures and magnetite geochemistry. Econ Geol 89:820–839

Nyström JO, Billström K, Henríquez F, Fallick AE, Naslund HR (2008) Oxygen isotope composition of magnetite in iron ores of the Kiruna type in Chile and Sweden. GFF 130:177–188

Ovalle JT, La Cruz NL, Reich M, Barra F, Simon AC, Konecke BA, Rodriguez-Mustafa MA, Deditius AP, Childress TM, Morata D (2018) Formation of massive iron deposits linked to explosive volcanic eruptions. Sci Rep 8:1–11

Parák T (1975) The origin of the Kiruna iron ores. Sveriges Geologiska Undersokning

Pearce JA, Harris NB, Tindle AG (1984) Trace element discrimination diagrams for the tectonic interpretation of granitic rocks. J Petrol 25:956–983

Pecoits E, Gingras MK, Barley ME, Kappler A, Posth NR, Konhauser KO (2009) Petrography and geochemistry of the Dales Gorge banded iron formation: Paragenetic sequence, source and implications for palaeo-ocean chemistry. Precambr Res 172:163–187

Peters ST, Alibabaie N, Pack A, McKibbin SJ, Raeisi D, Nayebi N, Torab F, Ireland T, Lehmann B (2020) Triple oxygen isotope variations in magnetite from iron-oxide deposits, central Iran, record magmatic fluid interaction with evaporite and carbonate host rocks. Geology 48:211–215

Philpotts AR (1967) Origin of certain iron-titanium oxide and apatite rocks. Econ Geol 62:303–315

Piccoli PM, Candela PA (2002) Apatite in igneous systems. Rev Miner Geochem 48:255–292

Porter TM (2011) Advances in the understanding of IOCG and related deposits. Hydrothermal iron oxide copper–gold and related deposits: a global perspective, vol 3. PGC Publishing, Adelaide, pp 1–109

Ramezani J (1997) Regional geology, geochronology and geochemistry of the igneous and metamorphic rock suites of the Saghand area, Central Iran. PhD thesis, St. Louis, Missouri, Washington University, USA, pp 1–416

Ramezani J, Tucker RD (2003) The Saghand region, Central Iran: U–Pb geochronology, petrogenesis and implications for Gondwana tectonics. Am J Sci 303:622–665

Ray GE, Webster ICL (2007) Geology and chemistry of the low Ti magnetite-bearing Heff Cu–Au skarn and its associated plutonic rocks, Heffley Lake, south-central British Columbia. Explor Min Geol 16:159–186

Reguir EP, Chakhmouradian AR, Halden NM, Yang P, Zaitsev AN (2008) Early magmatic and reaction-induced trends in magnetite from the carbonatites of Kerimasi, Tanzania. Can Mineral 46:879–900

Roberts DE, Hudson GRT (1983) The Olympic Dam copper–uranium–gold deposit, Roxby Downs, South Australia. Econ Geol 78:799–822

Roeder PL, MacArthur D, Ma XP, Palmer GR, Mariano AN (1987) Cathodoluminescence and microprobe study of rare-earth elements in apatite. Am Miner 72:801–811

Rojas PA, Barra F, Deditius A, Reich M, Simon A, Roberts M, Rojo M (2018) New contributions to the understanding of Kiruna-type iron oxide-apatite deposits revealed by magnetite ore and gangue mineral geochemistry at the El Romeral deposit, Chile. Ore Geol Rev 93:413–435

Rusk B, Oliver N, Cleverley J, Blenkinsop T, Zhang D, Williams P, Habermann P (2010) Physical and chemical characteristics of the Ernest Henry iron oxide copper gold deposit. In: Porter TM (ed) Hydrothermal iron oxide copper-gold and related deposits: a global perspective. PGC Publishing, Adelaide, pp 201–218

Sahandi M, Baumgartner S, Schmidt K (1984) Contributions to the stratigraphy and tectonics of the Zeber-Kuh range (east Iran). Neues Jahrbuch für Geologie und Paläontologie Abhandlungen 168:345–357

Samani BA (1988) Metallogeny of the Precambrian in Iran. Precambr Res 39:85–106

Samani B (1993) Saghand formation, a riftogenic unit of the upper Precambrian in Central Iran. Geosci Q J 2:32–45 ((**Persian with English abstract**))

Sarlus Z, Andersson UB, Martinsson O, Bauer TE, Wanhainen C, Andersson JB, Whitehouse MJ (2020) Timing and origin of the host rocks to the Malmberget iron oxide-apatite deposit, Sweden. Precambr Res 342:105652

Sawyer EW (2010) Migmatites formed by water-fluxed partial melting of a leucogranodiorite protolith: microstructures in the residual rocks and source of the fluid. Lithos 116:273–286

Sha LK, Chappell BW (1999) Apatite chemical composition, determined by electron microprobe and laser-ablation inductively coupled plasma mass spectrometry, as a probe into granite petrogenesis. Geochim Cosmochim Acta 63:3861–3881

Shao WY, Chung SL, Chen WS, Lee HY, Xie LW (2015) Old continental zircons from a young oceanic arc, eastern Taiwan: implications for Luzon subduction initiation and Asian accretionary orogeny. Geology 43:479–482

Simon AC, Knipping J, Reich M, Barra F, Deditius AP, Bilenker L, Childress T (2018) Kiruna-type iron oxide-apatite (IOA) and iron oxide copper-gold (IOCG) deposits form by a combination of igneous and magmatic-hydrothermal processes: evidence from the chilean iron belt. In: SEG 2018: Metals, Minerals, and Society. Keystone, Colorado, USA, pp 22–25

Sláma J, Košler J, Condon DJ, Crowley JL, Gerdes A, Hanchar JM, Horstwood MS, Morris GA, Nasdala L, Norberg N, Schaltegger U (2008) Plešovice zircon–a new natural reference material for U–Pb and Hf isotopic microanalysis. Chem Geol 249:1–35

Soheili M, Mahdavi M (1991) Geological Map of Esfordi: Tehran. Geol Surv Iran, scale 1(100):000

Stöcklin J (1968) A review of the structural geology and tectonics of Iran. Bull Am Assoc Petrol Geol 52:1228–1258

Stosch HG, Romer RL, Daliran F, Rhede D (2011) Uranium–lead ages of apatite from iron oxide ores of the Bafq District, East-Central Iran. Miner Depos 46:9–21

Sun SS, McDonough WF (1989) Chemical and isotopic systematics of oceanic basalts: implications for mantle composition and processes. Geol Soc Lond Spec Publ 42:313–345

Sun W, Yuan F, Jowitt SM, Zhou T, Liu G, Li X, Wang F, Troll VR (2019) In situ LA–ICP–MS trace element analyses of magnetite: genetic implications for the Zhonggu orefield, Ningwu volcanic basin, Anhui Province, China. Mineral Depos 54(8):1243–1264

Sverjensky DA (1984) Europium redox equilibria in aqueous solution. Earth Planet Sci Lett 67:70–78

Takin M (1972) Iranian geology and continental drift in the Middle East. Nature 235:147–150

Taylor HP (1967) Oxygen isotope studies of hydrothermal mineral deposits. In: Barnes HL (ed) Geochemistry of hydrothermal ore deposits. Holt, Rinehart and Winston Inc., New York, pp 109–142

Taylor HP (1968) The oxygen isotope geochemistry of igneous rocks. Contrib Miner Petrol 19:1–71

Toplis MJ, Corgne A (2002) An experimental study of element partitioning between magnetite, clinopyroxene and iron-bearing silicate liquids with particular emphasis on vanadium. Contrib Miner Petrol 144:22–37

Toplis MJ, Dingwell DB (1996) The variable influence of P2O5 on the viscosity of melts of differing alkali/aluminium ratio: Implications for the structural role of phosphorus in silicate melts. Geochim Cosmochim Acta 60:4107–4121

Torab FM (2008) Geochemistry and metallogeny of magnetite apatite deposits of the Bafq Mining District, Central Iran. PhD thesis, TU Clausthal, Germany, pp 1–131

Torab FM, Lehmann B (2007) Magnetite-apatite deposits of the Bafq district, Central Iran: apatite geochemistry and monazite geochronology. Miner Mag 71:347–363

Tornos F, Velasco F, Hanchar JM (2017) The magmatic to magmatic-hydrothermal evolution of the El Laco deposit (Chile) and its implications for the genesis of magnetite-apatite deposits. Econ Geol 112:1595–1628

Troll VR, Weis F, Jonsson E, Andersson UB, Majidi SA, Högdahl K, Harris C, Millet MA, Chinnasamy SS, Kooijman E, Nilsson KP (2019) Global Fe–O isotope correlation reveals magmatic origin of Kiruna-type apatite-iron-oxide ores. Nat Commun 10:1712

Valizadeh MV, Sharifi A (2004) Geochemical study of "Arash Syenite" (Central Iran) with special emphasis on alkali metasomatism. Geosciences 12:2–15

Vapnik Y, Bushmin S, Chattopadhyay A, Dolivo-Dobrovolsky D (2007) Fluid inclusion and mineralogical study of vein-type apatite ores in shear zones from the Singhbhum metallogenetic province, West Bengal, India. Ore Geol Rev 32:412–430

Verdel C, Wernicke BP, Ramezani J, Hassanzadeh J, Renne PR, Spell TL (2007) Geology and thermochronology of Tertiary Cordilleran-style metamorphic core complexes in the Saghand region of central Iran. Geol Soc Am Bull 119:961–977

Westhues A, Hanchar JM, Whitehouse MJ, Martinsson O (2016) New constraints on the timing of host-rock emplacement, hydrothermal alteration, and iron oxide-apatite mineralization in the Kiruna district, Norrbotten, Sweden. Econ Geol 111:1595–1618

Westhues A, Hanchar JM, LeMessurier MJ, Whitehouse MJ (2017) Evidence for hydrothermal alteration and source regions for the Kiruna iron oxide–apatite ore (northern Sweden) from zircon Hf and O isotopes. Geology 45:571–574

Westhues A, Hanchar JM, Voisey CR, Whitehouse MJ, Rossman GR, Wirth R (2017) Tracing the fluid evolution of the Kiruna iron oxide apatite deposits using zircon, monazite, and whole rock trace elements and isotopic studies. Chem Geol 466:303–322

Williams GJ, Houshmandzadeh A (1966) A petrological and genetic study of the Choghart iron ore body and the surrounding rocks. Geological Survey of Iran, Tehran, p 18

Williams PJ, Barton MD, Johnson DA, Fontboté L, De Haller A, Mark G, Oliver NHS, Marschik R (2005) Iron oxide copper–gold deposits: geology, space-time distribution, and possible modes of origin. Econ Geol 371–405

Wood SA (1990a) The aqueous geochemistry of the rare-earth elements and yttrium: 1. Review of available low-temperature data for inorganic complexes and the inorganic REE speciation of natural waters. Chem Geol 82:159–186

Wood SA (1990b) The aqueous geochemistry of the rare-earth elements and yttrium: 2. Theoretical predictions of speciation in hydrothermal solutions to 350 C at saturation water vapor pressure. Chem Geol 88:99–125

Yang F, Mao J, Liu F, Chai F, Geng X, Zhang Z, Guo X, Liu G (2013) A review of the geological characteristics and mineralization history of iron deposits in the Altay orogenic belt of the Xinjiang, Northwest China. Ore Geol Rev 54:1–16

Yassaghi A, Masoodi M (2011) A metamorphic core complex model for the host of uranium mineralization in the Khoshoumi Mountain, central Iran. Resour Geol 61:259–269

Yu J, Chen Y, Mao J, Pirajno F, Duan C (2011) Review of geology, alteration and origin of iron oxide–apatite deposits in the Cretaceous Ningwu basin, Lower Yangtze River Valley, eastern China: implications for ore genesis and geodynamic setting. Ore Geol Rev 43:170–181

Yuan H, Gao S, Liu X, Li H, Günther D, Wu F (2004) Accurate U-Pb age and trace element determinations of zircon by laser ablation-inductively coupled plasma-mass spectrometry. Geostand Geoanalyt Res 28:353–370

Zhang Z, Hong W, Jiang Z, Duan S, Li F, Shi F (2014) Geological characteristics and metallogenesis of iron deposits in western Tianshan, China. Ore Geol Rev 57:425–440

Zhou T, Fan Y, Yuan F, Zhang L, Qian B, Ma L, Yang X (2013) Geology and geochronology of magnetite–apatite deposits in the Ning-Wu volcanic basin, eastern China. J Asian Earth Sci 66:90–107